A POSSIBLE APPROACH TO THREE-DIMENSIONAL COSMIC-RAY PROPAGATION IN THE GALAXY. IV. ELECTRONS and ELECTRON-INDUCED γ-RAYS
(To appear in ApJ, December 2010)

T. Shibata, T. Ishikawa, and S. Sekiguchi

Department of Physics and Mathematics, Aoyama-Gakuin University, Kanagawa 229-8558, Japan

ABSTRACT

Based on the diffusion-halo model for cosmic-ray (CR) propagation, including stochastic reacceleration due to collisions with hydromagnetic turbulence, we study the behavior of the electron component and the diffuse γ-rays (Dγ's) induced by them. The galactic parameters appearing in these studies are essentially the same as those appearing in the hadronic CR components, while we additionally need information on the interstellar radiation field, taking into account dependences on both the photon energy, $E_{\rm ph}$, and the position, $\boldsymbol{r}$. We compare our numerical results with the data on hadrons, electrons and Dγ's, including the most recent results from FERMI, which gives two remarkable results; 1) the electron spectrum falls with energy as E_e^{-3} up to $1\,{\rm TeV}$, and does not exhibit prominent spectral features around $500\,{\rm GeV}$, in contrast to the dramatic excess appearing in both ATIC and PPB-BETS spectra, and 2) the EGRET GeV-excess in the Dγ spectrum is due neither to an astronomical origin (much harder CR spectrum in the galactic center) nor a cosmological one (dark matter annihilation or decay), but due to an instrumental problem. In the present paper, however, we focus our interest rather conservatively upon the internal relation between these three components, using *common* galactic parameters. We find that they are in reasonable harmony with each other within both the theoretical and experimental uncertainties, apart from the electron-anomaly problem, while some enhancement of Dγ's appears in the high galactic latitude with $|b| > 60°$ in the GeV region.

Subject headings: cosmic rays — Galaxy: structure — electrons: diffuse background

1. Introduction

Although the electron component is only a small fraction of all cosmic-ray (CR) components, around 1% of the proton intensity around 10 GeV, it plays a key role in understanding the structure of our Galaxy and the galactic phenomena occurring within it. This is because electrons have electromagnetic interactions with the interstellar radiation field, such as photons and magnetic fields, resulting in drastic energy loss during propagation through the Galaxy, in contrast to the hadronic component.

This peculiar nature yields valuable information for the study of CR astrophysics, which can not be obtained by the hadronic components alone. Namely, due to the rapid energy-loss rate, proportional to E_e^2 in the high energy region, from the inverse Compton scattering off photons and synchrotron radiation in magnetic fields, the life-time of TeV electrons is at most 10^5 yr, indicating that detected electrons have originated in nearby sources, less than 1 kpc from the solar system (SS). Therefore, accurate observations of TeV electrons will provide a direct signature of nearby CR sources as well as the mechanism of the CR acceleration, while depending on the release time from supernova remnants and their distance from the SS.

Qualitative studies of such a possibility have been performed by many authors (Shen 1970; Nishimura et al. 1979; Cowsik & Lee 1979; Berezinskii et al. 1990; Aharonian et al. 1995; Ptuskin & Ormes 1995; Pohl & Esposito 1998; Kobayashi et al. 2004; Delahaye et al. 2010), with Kobayashi et al. and Delahaye et al. presenting explicitly several candidates for nearby sources of high energy CR electrons, based on the most recent data for the age and distance of each supernova remnant near the SS, although the statistics of high energy electron data are currently too poor to identify sources definitely.

Particle identification and the energy determination of high energy electrons is, however, quite difficult, while direct observation of low energy electrons is relatively easy using, for instance, magnetic spectrometers, and has been performed by several groups (Golden et al. 1994; Boezio et al. 2000; DuVernois et al. 2001; Aguilar et al. 2002).

Although the statistics are not sufficient, the only group that succeeded in observing *directly* TeV electrons is Nishimura et al. (1980; see also Kobayashi et al. 1999) with the use of the balloon-borne emulsion chamber. It should be noted that they actually observe event by event the vertex point of the electron with subsequent $e^{\pm}$-pair due to bremsstrahlung γ, with no uncertainty from proton contamination. The precision in the energy determination is approximately 10% for electrons in the energy region larger than 50 GeV, based on both the three-dimensional cascade theory (Nishimura 1964) and the simulations (Kasahara 1985; Okamoto & Shibata 1987), which have been well established by the use of accelerator beams

(Hotta et al. 1980; Sato & Sugimoto 1979).

Recent development in high energy electron observations is indeed remarkable, particularly those of ATIC (Chang et al. 2008) and PPB-BETS (Torii et al. 2006), which showed an anomaly in the electron spectrum with a significant bump around $500\,\mathrm{GeV}$. Both groups point out that the excess indicates either a nearby source of energetic electrons, or those coming from the annihilation of dark matter particles.

On the other hand, the most recent results obtained by the FERMI Large Area Telescope (FERMI-LAT; Abdo et al. 2009) present no prominent excess, with the electron spectrum falling with energy as $E_e^{-3.04}$ up to $1\,\mathrm{TeV}$, which is not inconsistent with the emulsion chamber data (Kobayashi et al. 1999) within the statistical errors. The H.E.S.S. ground-based telescope (Aharonian et al. 2008, 2009) also shows no indication of structure in the electron spectrum, but rather a power-law spectrum with $E_e^{-3.0\pm0.1\pm0.3}$ (0.1: stat. error, 0.3: syst. error), albeit this being an indirect observation.

Nevertheless, looking carefully FERMI data around the anomaly-energy, they still show systematically an enhancement as large as 30% compared to the numerical results (Abdo et al. 2009; Strong et al. 2004; see also Figure 14 in this paper), so that we can not exclude the possibility of an additional component such as local sources and/or the dark matter scenario, while strength of the anomaly compared to the background *diffuse* electrons is not as dramatic as presented by ATIC and PPB-BETS.

In any case, both observational and theoretical studies for high energy electrons are becoming increasingly important not only for astrophysics, but also for particle physics and cosmology. It is, therefore, desirable to find a reasonable model for electron propagation in the Galaxy, which must explain consistently and simultaneously all CR observables and not just electrons, using common galactic parameters with the smallest number of variables possible. In the sense, the recent review article by Strong, Moskalenko, & Ptuskin (2007) is a useful survey of both the theory and relevant experimental data for the propagation of CRs, comprehensively summarizing the current landscape and open questions, although it was published just before the anomaly problem mentioned above.

Under these situations, we have studied the three-dimensional CR propagation model analytically, and found excellent agreement with the experimental data for various hadronic components, stable primaries, secondaries such as boron and sub-iron elements ($Z =21$–23), isotopes such as ^{10}Be, and antiprotons as well, in four papers, (Shibata et al. 2004, 2006, 2007a, 2008), hereafter referred to as Papers I, II, III and IV, respectively.

We have applied our model further to the studies of diffuse γ-rays (Dγ's) (Shibata, Honda, & Watanabe 2007b; hereafter Paper V), and found that all these components are

generally in agreement with each other using the same galactic parameters, within the uncertainties in the experimental data and various kinds of cross-sections used for the numerical calculations. However, in Paper V, we use the simulation results for electron-induced γ-rays provided by Hunter et al. (Bertsch et al. 1993; Hunter et al. 1997), where the modeling of CR propagation and the galactic parameters assumed are somewhat different from ours. So we have yet to see complete internal consistency among all CR components — hadrons, electrons and Dγ's — using the *same* galactic parameters in our propagation model.

In the present paper, we extend it to the electron component, based on the diffusion-halo model proposed by Ginzburg, Khazan & Ptuskin (1980), taking the reacceleration process into account. However, we focus in the present work on *diffuse* electrons in the steady state without discriminating those produced by nearby sources from those of distant ones, and present the intensity of the Dγ's produced by them in the energy range, $E_\gamma = 30\,\mathrm{MeV}-100\,\mathrm{GeV}$, covered by EGRET and FERMI. Comparison with radio and TeV-γ data will be reported separately in the near future.

In order to apply our model to the electron component and electron-induced Dγ's, we need information on the interstellar radiation field (ISRF) in addition to the interstellar matter (ISM), particularly their spatial gradients for the study of the (l, b)-distribution of Dγ's (l: galactic longitude; b: galactic latitude). Nowadays the most advanced and standard code for the ISM and ISRF models is GALPROP, extensively developed by Strong & Moskalenko (1998), incorporating the latest survey data in the very wide wavelength range from ultraviolet to radio. In the present work, we assume empirical density distributions for the ISM and ISRF, smoothing the numerical data given by GALPROP available most recently (Porter et al. 2008), in order to combine with our analytical solution for electron-induced Dγ's.

In §2, we discuss the interstellar environment provided by GALPROP, focusing on the spatial distribution of both matter (atomic, molecular, and ionized hydrogen) and photons (ultraviolet, visible, infrared, mid- and far-infrared, and cosmic microwave background [CMB] radiations), and in §3 we present the relevant elementary processes for electrons, focussing on the energy losses due to ionization, bremsstrahlung, synchrotron, inverse Compton (IC), and on the energy gain due to the reacceleration.

In §4, we present the diffusion equation, and give its solution explicitly in the steady state, $N_e(\boldsymbol{r}; E_e)$, where the Klein-Nishina effect is quite important in the electron energy spectrum in the high energy region, $\gtrsim 10\,\mathrm{GeV}$. In §5, we present the emissivity of electron-induced γ's, $q_\gamma(\boldsymbol{r}; E_\gamma)$, with use of realistic spatial distributions of ISM and ISRF as discussed in §2, and show the numerical results at several observational points, where those of the hadron-induced γ's are presented as well. In §6, we first summarize the galactic parameters and their explicit values expected from the CR data, and then compare our numerical results

of electron flux and Dγ's with recent observational data, including those most recently obtained by FERMI and H.E.S.S. Finally in §7, we summarize the results, and discuss several remaining open questions, while we do not touch upon the so called electron-anomaly.

2. Interstellar environment of our Galaxy

2.1. Interstellar matter

First we consider the ISM for two processes, ionization and bremsstrahlung. In Figure 1 we plot histograms of column density for HI and H_2 in the galactic plane (GP) given by GALPROP, where we also plot the empirical curves used in the present work,

$$-\ln\rho_{\mathrm{HI}}(r) = P_{\mathrm{HI}}^{(0)} + P_{\mathrm{HI}}^{(1)}r + P_{\mathrm{HI}}^{(2)}\ln r + P_{\mathrm{HI}}^{(3)}r^{\frac{1}{2}}, \tag{1a}$$

$$-\ln\rho_{\mathrm{H_2}}(r) = P_{\mathrm{H_2}}^{(0)} + P_{\mathrm{H_2}}^{(1)}r + P_{\mathrm{H_2}}^{(2)}\ln r + P_{\mathrm{H_2}}^{(3)}r^{2}, \tag{1b}$$

with r in kpc, and ρ_h ("h" $\equiv$ HI, H_2) in 10^{20} H atoms cm^{-2}. The numerical values of the coefficients are summarized in Table 1. However, the choice of above empirical form is not critical, and other choices may be possible.

The H_2 gas is strongly confined to the GP and its vertical structure is modeled by a gaussian distribution with a width of approximately 70 pc, while the HI gas lies in a flat layer with a FWHM of 230 pc in 3.5 kpc $< r < r_\odot$ (=8.5 kpc), and is approximated by the sum of two gaussians and an exponential tail (Ferriere 2001; Moskalenko et al. 2002). Taking
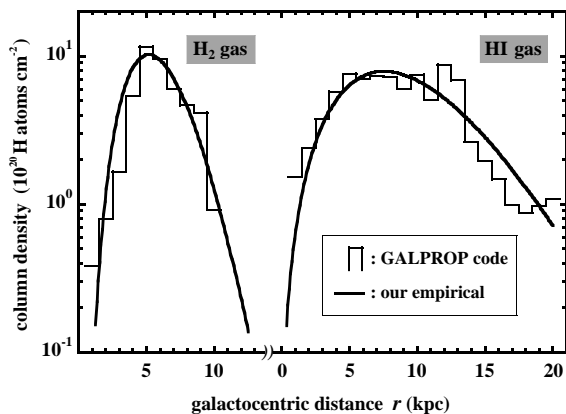

Fig. 1.— Column density of interstellar hydrogen. Curves are empirical ones given by equation (1) with the parameterization summarized in Table 1.

Table 1. Summary of the numerical values of the coefficients appearing in equations (1a) and (1b) in units of $10^{20} H \, atoms \, cm^{-2}$, where "$(\pm m)$" denotes the multiplication of $10^{\pm m}$.

$P_{HI}^{(0)}$	$P_{HI}^{(1)}$	$P_{HI}^{(2)}$	$P_{HI}^{(3)}$	$P_{H_2}^{(0)}$	$P_{H_2}^{(1)}$	$P_{H_2}^{(2)}$	$P_{H_2}^{(3)}$
3.862(+0)	7.903(−1)	−9.426(−2)	−4.261(+0)	1.848(+0)	8.339(−1)	−5.560(+0)	2.405(−2)

Table 2. Summary of functions for ISM gas density, H I and H_2, where r, $r_\odot$ (=8.5kpc), z, and z_0 are all in units of kpc, and $n_h^\odot$ in units of $H \, atoms \, cm^{-3}$.

"h"	$n_h^\odot$	$\Xi_h(r, z)$
H I	0.57	$\dfrac{1}{0.065\sqrt{\pi} + 0.160}\left\{0.4\exp\left[-\left(\dfrac{z}{0.12}\right)^2\right] + 0.2\exp\left[-\left(\dfrac{z}{0.35}\right)^2\right] + 0.4\exp\left(-\dfrac{z}{0.40}\right)\right\}$
H_2	0.53	$\dfrac{1}{0.036\sqrt{\pi} + 0.2z_0}\left\{\exp\left[-\left(\dfrac{z}{0.071}\right)^2\right] + 0.2\dfrac{z}{z_0}\exp\left(-\dfrac{z}{z_0}\right)\right\}; \; z_0(r) = 0.4\cosh\left(\dfrac{2r}{3r_\odot}\right)$

these situations into account, we assume the following spatial distribution for the ISM gas density, corresponding to equations (1a) and (1b),

$$\frac{n_h(\boldsymbol{r})}{n_h^{\odot}} = \frac{\Xi_h(r,z)}{\Xi_h(r_{\odot},0)}\frac{\rho_h(r)}{\rho_h(r_{\odot})}, \quad (\text{``}h\text{''} \equiv \mathrm{H\,I,\ H_2}),$$ (2)

where $n_{\mathrm{HI}}^{\odot}$ ($n_{\mathrm{H_2}}^{\odot}$) is the gas density of $\mathrm{H\,I}$ ($\mathrm{H_2}$) at the SS with typically $n_{\mathrm{HI}}^{\odot} \approx n_{\mathrm{H_2}}^{\odot} \approx 0.5$ $\mathrm{H\,atoms\,cm^{-3}}$. See Table 2 for the explicit forms of Ξ_{HI} and $\Xi_{\mathrm{H_2}}$.

For the ionized hydrogen gas, $\mathrm{H\,II}$, we use the two-component model of Cordes et al. (1991), $n_{\mathrm{HII}}(\boldsymbol{r}) = n_{\mathrm{HII}}^{(1)}(\boldsymbol{r}) + n_{\mathrm{HII}}^{(2)}(\boldsymbol{r})$, and both components are modeled by a gaussian-type distribution for the radial structure, and by a simple exponential one for the vertical structure. The explicit values of the two components at the SS, $[n_{\mathrm{HII}}^{(1)}(r_{\odot}), n_{\mathrm{HII}}^{(2)}(r_{\odot})]$, are $[0.025, 0.013]\,\mathrm{cm^{-3}}$ respectively (Cordes et al. 1991; Strong et al. 1998). So the contribution of $\mathrm{H\,II}$ is much smaller than those of $\mathrm{H\,I}$ and $\mathrm{H_2}$ and is not important in the present work.

2.2. Interstellar radiation field

First we consider the medium — virtual photons induced by the static magnetic field — for the synchrotron process. It is approximately given by an exponential-type gradient, while the scale height is not yet clear. Practically, for the study of synchrotron radiation, we need the *energy density* of virtual photons at $\boldsymbol{r}$, $\epsilon_{\mathrm{B}}(\boldsymbol{r})$, and assume in the present work

$$\epsilon_{\mathrm{B}}(\boldsymbol{r}) = \epsilon_{\mathrm{B},0}\exp[-(r/r_{\mathrm{B}} + |z|/z_{\mathrm{B}})],$$ (3)

with

$$\epsilon_{\mathrm{B},0} = B_0^2/8\pi,$$

where B_0 is the magnetic field at the galactic center (GC), and $\epsilon_{\mathrm{B},0}$ is its energy density, for instance $\epsilon_{\mathrm{B},0} \approx 1\,\mathrm{eVcm^{-3}}$ for $B_0 = 6\,\mu\mathrm{G}$, and typically $[2r_{\mathrm{B}}, 2z_{\mathrm{B}}] \approx [10,\ 2]\,\mathrm{kpc}$ (Strong et al. 2000).

On the other hand, the photon gas for the IC process is somewhat different from those discussed above. Namely, we need the number density of the photon gas in the ISRF, $n_{\mathrm{ph}}(\boldsymbol{r}; E_{\mathrm{ph}})$, as a function of the target photon energy E_{ph} at $\boldsymbol{r}$. Separating it into two parts, a $\boldsymbol{r}$-dependent energy-density term, $\epsilon_{\mathrm{ph}}(\boldsymbol{r})$, and a $\boldsymbol{r}$-independent term, $W_{\mathrm{ph}}(k)$ with $k = E_{\mathrm{ph}}/[k_{\mathrm{B}}T_{\mathrm{ph}}]$, we rewrite $n_{\mathrm{ph}}(\boldsymbol{r}; E_{\mathrm{ph}})$ as

$$E_{\mathrm{ph}}n_{\mathrm{ph}}(\boldsymbol{r};E_{\mathrm{ph}})dE_{\mathrm{ph}} = \epsilon_{\mathrm{ph}}(\boldsymbol{r})W_{\mathrm{ph}}(k)d\ln k, \tag{4}$$

where k_{B} is the Boltzmann constant, and T_{ph} is the characteristic temperature of the ISRF.

There are three main radiation sources in the photon gas, (i) the $2.7\,\mathrm{K}$ CMB radiation, (ii) stellar radiation with wavelengths of 0.1–$10\,\mu\mathrm{m}$ (ultraviolet–visible–near-infrared), and (iii) re-emitted radiation from dust grains at 10-$1000\,\mu\mathrm{m}$ (mid-to-far–infrared).

We classify them further into six wavelength bands, each labeled with $i=0$ for (i), $i=1$, 2, 3 for stellar-1, -2, -3 in (ii), and $i=4$, 5 for dust-1, -2 in (iii) (see Fig. 2). Needless to say, there is no spatial gradient in the CMB ($i=0$), which is distributed uniformly in space, $\epsilon_{\mathrm{ph}}(\boldsymbol{r}) \equiv \epsilon_{\mathrm{ph}}^{(0)} = 0.261\,\mathrm{eVcm}^{-3}$, and the normalized spectrum, $W_{\mathrm{ph}}^{(0)}(k)$, is given by the familiar Planck formula with $T_{\mathrm{ph}} = 2.73\,\mathrm{K}$.

On the other hand, for (ii) and (iii) in the wavelength range $\lambda = 0.1$–$1000\,\mu\mathrm{m}$, the energy density, $\epsilon_{\mathrm{ph}}^{(i)}(\boldsymbol{r})$ ($i=1$–5), must depend on $\boldsymbol{r}$, and $W_{\mathrm{ph}}^{(i)}(k)$ is unlike the simple CMB spectrum, and is very complicated. In the following discussions, we often omit the suffix i for simplicity unless otherwise specified.

In the present work, we assume a gaussian-type distribution in $\ln k$ for $W_{\mathrm{ph}}(k)$,

$$W_{\mathrm{ph}}(k) = \frac{1}{\sqrt{2\pi}\sigma}\,\mathrm{e}^{-(\ln k)^2/(2\sigma^2)}; \quad k = \lambda_0/\lambda, \tag{5}$$

so that the mean radiation intensity, I_{ph}, is given by

$$\frac{4\pi\lambda I_{\mathrm{ph}}(\boldsymbol{r};\lambda)}{c\epsilon_{\mathrm{ph}}(\boldsymbol{r})} = \frac{1}{\sqrt{2\pi}\sigma}\exp\left[-\frac{[\ln(\lambda_0/\lambda)]^2}{2\sigma^2}\right], \tag{6}$$

where λ_0 is the peak wavelength for each radiation with $k_{\mathrm{B}}T_{\mathrm{ph}} = 2\pi c\hbar/\lambda_0$.

In Figure 2, we present examples of the mean radiation intensity (multiplied by $4\pi\lambda$) for the maximal metalicity gradient (*filled symbols*) and no metalicity gradient (*open symbols*) at two radial distances, $r=0$ (*squares*) and $8\,\mathrm{kpc}$ (*circles*) in the GP given by GALPROP, where also drawn are curves expected from the right-hand side of equation (6) for $W_{\mathrm{ph}}(k)$, assuming

$$\epsilon_{\mathrm{ph}}(\boldsymbol{r}) = \epsilon_{\mathrm{ph},0}\exp[-(r/r_{\mathrm{ph}} + |z|/z_{\mathrm{ph}})], \tag{7}$$

for $r \geq 3\,\mathrm{kpc}$, and see caption of Table 3 otherwise. In Table 3 we summarize numerical values of $[\lambda_0^{(i)}, T_i, \sigma_i; \epsilon_{\mathrm{ph},0}^{(i)}]$ ($i=0$–5) with $r_{\mathrm{ph}} = 3.2\,\mathrm{kpc}$ irrespective of the population i, and also presented are those of $\epsilon_{\mathrm{ph}}^{(i)}(r)$ for $r \leq 3\,\mathrm{kpc}$, while they are independent of r except $\epsilon_{\mathrm{ph}}^{(2)}(r)$.

Let us demonstrate the energy density separately for the stellar and the dust radiation, $\sum_{i=1}^{3}\epsilon_{\mathrm{ph}}^{(i)}$ and $\sum_{i=4}^{5}\epsilon_{\mathrm{ph}}^{(i)}$ respectively, against the galactocentric distance r in Figure 3, where
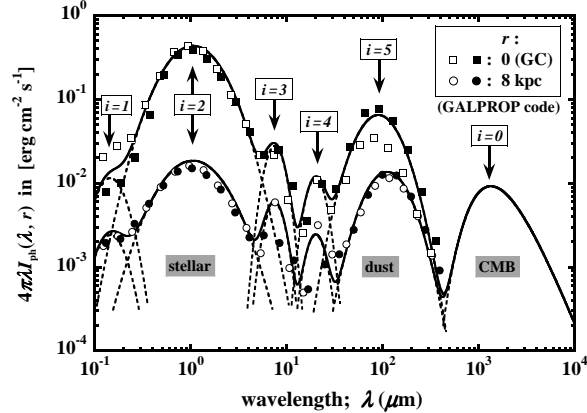
Fig. 2.— Interstellar radiation field (ISRF) at two galactocentric distances obtained by GALPROP, $r = 0$ (GC; *square symbols*) and 8 kpc (near SS; *circle symbols*). Open marks correspond to maximum metalicity gradient, and filled ones to the minimum metalicity gradient. Dotted curves are given by equation (6) with parameters summarized in Table 3 for each population i, while the solid ones are those superposing them. CMB radiation (*solid curve*) is also shown for reference.

we plot also numerical data given by Mathis et al. (1983; *filled grey symbols*). Two curves for the stellar emission and the dust re-emission are drawn by the use of the parameterization summarized in Table 3, where we do not take the difference in the choice of metalicity gradient into account, as it is effective only near the GC for the dust re-emission and is approximately one order of magnitude smaller than the stellar radiation.

For the latitudinal scale height, z_{ph}, in equation (7), we assume $z_{ph} \approx r_{ph}/8 = 0.4$ kpc, referring to the speculation by Freudenreich (1998) based on the DIRBE (Diffused Infrared Background Experiment) survey, while the surveys of the diffuse FIR/sub-mm emission for the latitudinal direction at various radial distances r are not sufficient to construct a reliable model.

3. Energy loss and gain

3.1. Energy loss in ISM and ISRF

The energy loss processes for the electron component are dramatically different from those for the hadronic components, with four main processes: bremsstrahlung ($\equiv$ "rad"),
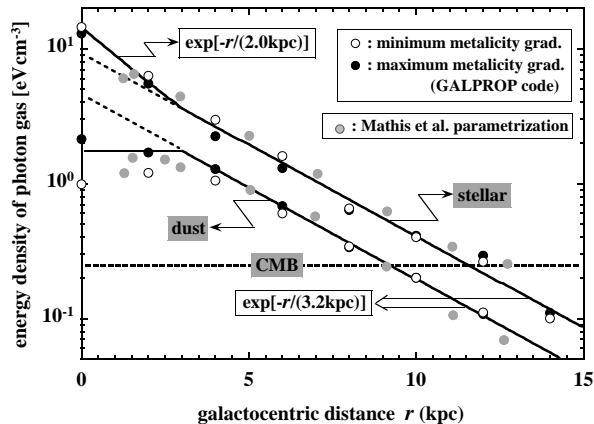
Fig. 3.— ISRF energy density as a function of galactocentric distance r at $z = 0$ for the stellar radiation and the re-emission from dust grains, each with the maximum metalicity gradient (*filled black circles*) and minimum metalicity gradient (*open circles*), where also shown are those obtained by Mathis et al. (1983) (*filled grey circles*). *Solid curves* are the empirical ones obtained by equation (7).

ionization ($\equiv$ "ion"), synchrotron and IC (together $\equiv$ "sic"). For the bremsstrahlung (Koch & Motz 1959; Gould 1969; Ginzburg 1979),

$$-\frac{1}{E_e}\Big\langle \frac{\Delta E_e}{\Delta t} \Big\rangle_{\mathrm{rad}} \simeq n(\boldsymbol{r})w_{\mathrm{rad}}(E_e)\Big[1 + O\Big(\frac{n_{\mathrm{HII}}}{n}\Big)\Big], \tag{8}$$

with

$$n(\boldsymbol{r}) = n_{\mathrm{HI}}(\boldsymbol{r}) + n_{\mathrm{HII}}(\boldsymbol{r}) + n_{\mathrm{H_2}}(\boldsymbol{r}), \tag{9}$$

where $w_{\mathrm{rad}}(E_e \gg m_e c^2) \equiv w_{\mathrm{rad}}^{(\infty)} \approx 7.30 \times 10^{-16}$ cm^{3}s^{-1}, independent of E_e with the complete screening cross-section in the high energy region; see Appendix A for the explicit forms of $w_{\mathrm{rad}}(E_e)$, and §2.1 for n_h, ("h" $\equiv$ HI, HII, H$_2$).

Similarly for the ionization, we use the Bethe-Bloch formula (Ginzburg 1979)

$$-\Big\langle \frac{\Delta E_e}{\Delta t} \Big\rangle_{\mathrm{ion}} \simeq n(\boldsymbol{r})w_{\mathrm{ion}}(E_e)\Big[1 + O\Big(\frac{n_{\mathrm{HII}}}{n}\Big)\Big], \tag{10}$$

with

$$w_{\mathrm{ion}}(E_e) = w_{\mathrm{ion}}^{(0)}\Big\{\ln[E_e/\mathrm{GeV}] + 13.8\Big\},$$

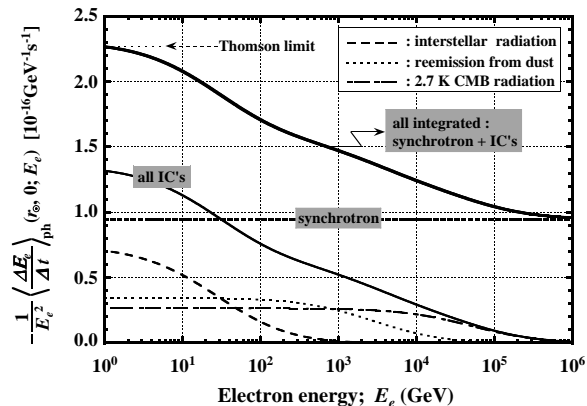and $w_{\mathrm{ion}}^{(0)} = 0.229 \times 10^{-16}$ cm^{3}s^{-1}.

Fig. 4.— Energy losses per unit time of CR electrons in ISRF at SS ($r_\odot = 8.5\,\mathrm{kpc}$), shown separately for four components, synchrotron (*heavy dotted line*), IC's by stellar radiation (*broken curve*), by re-emission from dust grains (*dotted curve*), and by CMB (*broken dotted curve*), together with the sums, IC-all $\equiv$ IC-stellar + IC-dust + IC-CMB (*thin solid curve*), and synchrotron + IC-all (*heavy solid curve*).

On the other hand, the energy losses due to the synchrotron (abbreviated as "SY" for subscripts appearing in the following equations) and IC are rather complicated, in addition to the energy dependent cross-section of the Klein-Nishina formula,

$$\left\langle \frac{\Delta E_e}{\Delta t} \right\rangle_{\mathrm{sic}} = \left\langle \frac{\Delta E_e}{\Delta t} \right\rangle_{\mathrm{SY}} + \left\langle \frac{\Delta E_e}{\Delta t} \right\rangle_{\mathrm{IC}}, \tag{11}$$

where

$$-\frac{1}{w_{\mathrm{T}} E_e^2} \left\langle \frac{\Delta E_e}{\Delta t} \right\rangle_{\mathrm{SY}} = \epsilon_{\mathrm{B}}(\boldsymbol{r}), \tag{12a}$$

$$-\frac{1}{w_{\mathrm{T}} E_e^2} \left\langle \frac{\Delta E_e}{\Delta t} \right\rangle_{\mathrm{IC}} = \sum_{i=0}^{5} \epsilon_{\mathrm{ph}}^{(i)}(\boldsymbol{r}) \Lambda(E_e, T_i), \tag{12b}$$

with $w_{\mathrm{T}} = 1.018 \times 10^{-16}\,\mathrm{cm^3 s^{-1}}$. See § 2.2 and Table 3 for $[T_i; \epsilon_{\mathrm{ph}}^{(i)}(\boldsymbol{r})]$ ($i = 0\text{–}5$), and $\Lambda(E_e, T_i)$ is given by equation (A6) in Appendix A, which comes from the Klein-Nishina cross-section. In Figure 4, we present the energy loss divided by E_e^2 at the SS against E_e separately for individual (virtual) photon fields as well as for superposed ones, $-\langle \Delta E_e / \Delta t \rangle_{\mathrm{sic}}^\odot / E_e^2$, where

we assume $B_\perp = 5\,\mu\mathrm{G}$, corresponding to $\epsilon_{\mathrm{B}}^\odot = 0.93\,\mathrm{eV cm^{-3}}$, for the magnetic field, and use $\epsilon_{\mathrm{ph}}^{(i)}(r_\odot)$ presented in the second line from the bottom of Table 3 with $r = r_\odot$ for the photon gas field.
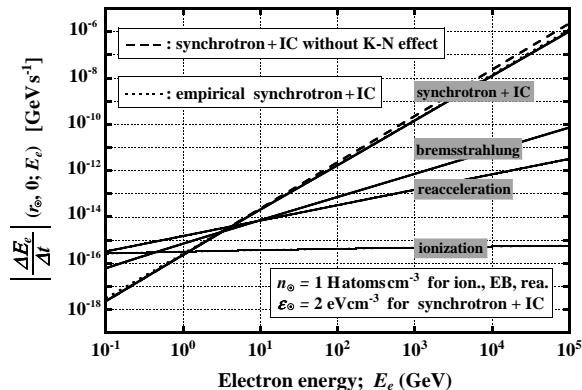
Fig. 5.— Energy losses per unit time of CR electrons in ISRF and ISM at SS $(r = r_\odot)$ as a function of electron energy, shown separately for four processes, synchrotron + IC, bremsstrahlung, reacceleration, and ionization. We present three curves for synchrotron + IC, with the solid one from the Klein-Nishina cross-section, the broken one from the Thomson cross-section, and the dotted one from the empirical one.

For $E_e \lesssim 1\,\mathrm{GeV}$, $\Lambda(E_e, T_i) \approx 1$, i.e., the Thomson cross-section is valid, so that equation (11) is separable in $\boldsymbol{r}$ and E_e, leading to a simple expression, $\epsilon(\boldsymbol{r})w_\mathrm{T}E_e^2$, with $\epsilon(\boldsymbol{r}) = \epsilon_\mathrm{B}(\boldsymbol{r}) + \sum_{i=0}^{5} \epsilon_\mathrm{ph}^{(i)}(\boldsymbol{r})$. In practice, we find it is well reproduced by the following form over a wide energy range

$$-\left\langle \frac{\Delta E_e}{\Delta t} \right\rangle_\mathrm{sic} \simeq \epsilon(\boldsymbol{r})w_\mathrm{T}E_e^{2-\delta}; \quad \delta = 0.075, \tag{13}$$

while $\epsilon(\boldsymbol{r})$ depends on E_e very weakly.

In Figure 5 we demonstrate the energy loss of individual processes separately, those due to "rad", "ion" and "sic" at the SS against the kinetic energy of the electron E_e with $\epsilon_\odot = 2\,\mathrm{eVcm}^{-3}$ and $n_\odot = 1\,\mathrm{H\,atoms\,cm}^{-3}$, where we plot the above empirical relationship (13) (*dotted curve*) and the energy gain due to the reacceleration ($\equiv$ "rea"; see next subsection) together. One finds that it reproduces satisfactorily the exact one (11) with equations (12a) and (12b).

3.2. Energy gain due to the reacceleration

In Paper II, we present the energy gain per unit time due to the reacceleration

$$\frac{1}{E_e}\left\langle \frac{\Delta E_e}{\Delta t} \right\rangle_\mathrm{rea} = n(\boldsymbol{r})w_\mathrm{rea}[E_e/\mathrm{GeV}]^{-\alpha}, \tag{14}$$

with

$$w_{\text{rea}} = c\zeta_0; \quad \zeta_0 \approx \frac{4}{9}\frac{v_M^2}{n_0^* c D_0^*}, \tag{15}$$

where $w_{\text{rea}} = 15.0 \times 10^{-16}\,\text{cm}^3\,\text{s}^{-1}$ in the case of, for instance, $\zeta_0 = 50$ millibarn (mbarn), corresponding to the choice of a parameter set with $v_M = 20\text{–}30\text{km}\,\text{s}^{-1}$ (Alfvén velocity), $n_0^* = 0.06\text{–}0.14\text{H atoms cm}^{-3}$, and $D_0^* = 2 \times 10^{28}\text{cm}^2\text{s}^{-1}$. The smallness of the gas density with $n_0^* \ll 1$ H atoms cm^{-3} indicates that the reacceleration process occurs even at some distance from the GP.

The fluctuation in the energy gain due to the reacceleration is given (Gaisser 1990; Paper II) by

$$\frac{1}{E_e^2}\left\langle \frac{\Delta E_e^2}{\Delta t} \right\rangle_{\text{rea}} = \frac{1}{2}n(\boldsymbol{r})w_{\text{rea}}[E_e/\text{GeV}]^{-\alpha}. \tag{16}$$

3.3. Total energy loss and gain

As discussed in the last two subsections, we have the total average energy-loss and the energy-gain per unit time

$$-\left\langle \frac{\Delta E_e}{\Delta t} \right\rangle_{\text{all}} = n(\boldsymbol{r})\mathcal{W}_n(E_e) + \epsilon(\boldsymbol{r})\mathcal{W}_\epsilon(E_e), \tag{17}$$

where

$$\mathcal{W}_n(E_e) = w_{\text{rad}}(E_e)E_e + w_{\text{ion}}(E_e) - w_{\text{rea}}E_e^{1-\alpha}, \tag{18a}$$

and

$$\mathcal{W}_\epsilon(E_e) \simeq w_{\text{T}}E_e^{2-\delta}; \quad \delta = 0.075. \tag{18b}$$

One might note from equation (18a) that there exist two energies, E_c^- and E_c^+, at which the first term proportional to $n(\boldsymbol{r})$ in the right-hand of equation (17) becomes null. In Figure 6, we demonstrate $\mathcal{W}_n(E_e)$ against several choices of ζ_0, and find $[E_c^-, E_c^+] \approx [0.1,\ 7]$ GeV in the case of $\zeta_0 = 50$ mbarn. Namely, the synchrotron-IC is dominant for $E_e \gtrsim E_c^+$, while the reacceleration is effective for $E_c^- \lesssim E_e \lesssim E_c^+$, and the ionization for $E_e \lesssim E_c^-$.

As discussed in §2, the total number density of the ISM gas, $n(\boldsymbol{r})$, and the total energy density of the ISRF, $\epsilon(\boldsymbol{r})$, have complicated spatial distributions coming from local irregularities, which are not yet well established. On the other hand, in our previous papers, we have assumed a simple exponential-type form for $n(\boldsymbol{r})$, smearing out the local irregularities,

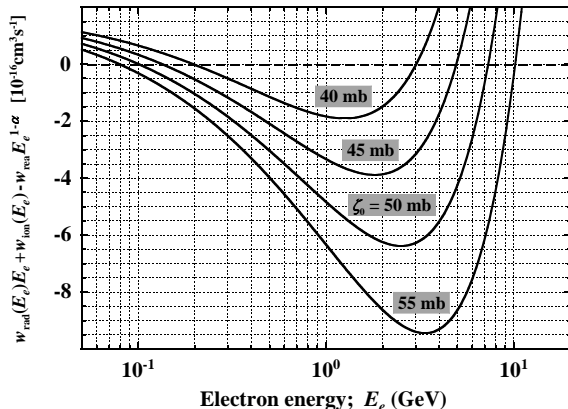$$\bar{n}(\boldsymbol{r}) = \bar{n}_0 \exp[-(r/r_n + |z|/z_n)], \tag{19}$$

Fig. 6.— Numerical values of $\mathcal{W}_n(E_e) \equiv w_{\mathrm{rad}}(E_e)E_e + w_{\mathrm{ion}}(E_e) - w_{\mathrm{rea}}E_e^{1-\alpha}$ against E_e for $\zeta_0 = 40$–55 mbarn, where the screening effect for w_{rad} is taken into account.

greatly simplifying the complicated distributions given by equations (1), (2) with Tables 1, 2, where $\bar{n}_0$ is the (*interpolated*) average gas density with approximately $1.5\,\mathrm{H}$ atoms cm^{-3} at the GC, and $[r_n, z_n] \approx [20, 0.2]$ kpc.

In spite of such a simplification, we have found that our model reproduces remarkably well the experimental data on *hadronic components*. This tells us that *charged* CR components are well mixed during their propagation in the Galaxy over a residence time of approximately 10^7 yr, effectively smearing the local inhomogeneous structure of the ISM. In fact, it is well established that the anisotropy amplitude of CRs is of the level of at most 10^{-3} at energies of 1–100 TeV (Sakakibara 1965; Nagashima et al. 1989; Cutler & Groom 1991). This is the reason why even the simplest leaky-box model and/or the simplified diffusion model such as, for instance, constant gas density and constant diffusion coefficient without spatial gradient, reproduces the CR hadronic components so well (Berezinskii et al. 1990).

Now, corresponding to the simplification (19) for $n(\boldsymbol{r})$, we assume the following simple exponential type form for $\epsilon(\boldsymbol{r})$ as well

$$\bar{\epsilon}(\boldsymbol{r}) = \bar{\epsilon}_0 \exp[-(r/r_\epsilon + |z|/z_\epsilon)], \tag{20}$$

where $\bar{\epsilon}_0$ is the (*interpolated*) average energy density of the ISRF at the GC, and two parameters, r_ϵ and z_ϵ, correspond to the scale heights for the spatial gradients, almost independent of the energy. Typically $[\bar{\epsilon}_0;\ r_\epsilon, z_\epsilon] \approx [16\,\mathrm{eVcm}^{-3};\ 4\,\mathrm{kpc}, 0.75\,\mathrm{kpc}]$ (Ishikawa 2010).

However, while the simplifications given by equations (19) and (20) are applied for electrons (and hadrons), we stress here that those presented in §2 are actually used for Dγ's as discussed in §6, namely $n_h(\boldsymbol{r})$ with "h" $\equiv$ H I, H II, H$_2$ for $n(\boldsymbol{r})$, and $\epsilon_{\mathrm{ph}}^{(i)}(\boldsymbol{r})$ ($i=0$–5) for

$\epsilon(\boldsymbol{r})$ with weak energy dependences in $\epsilon_{\mathrm{ph},0}^{(i)}$ as presented in Table 3. This is because Dγ's produced by CR hadrons and electrons are directly affected by the environment of ISM and ISRF around the birth site of the produced γ's.

4. Diffusion equation for electron component

4.1. Basic equation

The transport equation for the electron density, $N_e(\boldsymbol{r};E_e,t)$, is given by (Berezinskii et al. 1990),

$$\left[\frac{\partial}{\partial t} - \nabla \cdot D(\boldsymbol{r};E_e)\nabla + \Delta_E\right] \cdot N_e(\boldsymbol{r};E_e,t) = Q(\boldsymbol{r};E_e,t), \tag{21}$$

with

$$\Delta_E = \frac{\partial}{\partial E_e}\left\langle \frac{\Delta E_e}{\Delta t}\right\rangle_{\mathrm{all}} - \frac{1}{2}\frac{\partial^2}{\partial E_e^2}\left\langle \frac{\Delta E_e^2}{\Delta t}\right\rangle_{\mathrm{rea}}, \tag{22}$$

see equations (19) and (20) for the *average* energy-loss (-gain) in the all processes, with the replacement of $[n(\boldsymbol{r}),\epsilon(\boldsymbol{r})]$ in equation (17) by $[\bar{n}(\boldsymbol{r}),\bar{\epsilon}(\boldsymbol{r})]$, and equation (16) for the fluctuation of the energy gain in the reacceleration process respectively. For the diffusion coefficient and the source spectrum, we assume (note $v \approx c$, and $R_e \approx E_e$)

$$D(\boldsymbol{r};E_e) = E_e^\alpha D(\boldsymbol{r}), \quad Q(\boldsymbol{r};E_e,t) = E_e^{-\gamma}Q(\boldsymbol{r};t), \tag{23}$$

with

$$D(\boldsymbol{r}) = D_0 \exp(r/r_D + |z|/z_D), \tag{24a}$$

$$Q(\boldsymbol{r};t) = Q_0(t)\exp[-(r/r_Q + |z|/z_Q)]. \tag{24b}$$

In Table 4, we summarize parameters related to the scale heights, $r_D, z_D, \dots$, which often appear in the present paper.

Now, remembering $\mathcal{W}_\epsilon(E_e) \gg \mathcal{W}_n(E_e)$ in the high energy (HE) region, say, $E_e \gtrsim E_c^+$ ($\approx 7\,\mathrm{GeV}$), and vice versa in the low energy (LE) region, $E_e \lesssim E_c^+$, the energy loss given by equation (17) is written as

$$-\left\langle \frac{\Delta E_e}{\Delta t}\right\rangle_{\mathrm{all}} \simeq \begin{cases} \bar{\epsilon}(\boldsymbol{r})\mathcal{W}_\epsilon(E_e) + O[\bar{n}(\boldsymbol{r})\mathcal{W}_n(E_e)]; & E_e \gtrsim E_c^+, \tag{25a}\\[2ex] \bar{n}(\boldsymbol{r})\mathcal{W}_n(E_e) + O[\bar{\epsilon}(\boldsymbol{r})\mathcal{W}_\epsilon(E_e)]; & E_e \lesssim E_c^+, \tag{25b} \end{cases}$$

Table 3. Summary of the numerical values of $[\lambda_0^{(i)}(\mu m), T_i(K), \sigma_i]$, and those of $\epsilon_{\rm ph,0}^{(i)}(eVcm^{-3})$ for $r \geq 3$kpc in the second line from the bottom, and $\epsilon_{\rm ph}^{(i)}(eV\,cm^{-3})$ for $r \leq 3$kpc in the bottom line, where $\lambda_0^{(5)}$, $T_5(K)$, and σ_2 have weak r-dependence as shown in remarks with r in kpc, while $\epsilon_{\rm ph}^{(i)}$ are independent of r except $\epsilon_{\rm ph}^{(2)}$. The numerical value of 13.9 in $\epsilon_{\rm ph}^{(2)}$ corresponds to the energy density of the stellar radiation for the population $i = 2$ at GC (see Figure 2). See also equation (7) for $\epsilon_{\rm ph,0}^{(i)}$ and $\epsilon_{\rm ph}^{(i)}(r)$ for $r \geq 3$kpc.

	$i = 0$	$i = 1$	$i = 2$	$i = 3$	$i = 4$	$i = 5$	remarks (r-dependence)
$\lambda_0^{(i)}$	1.06(+3)	1.45(−1)	1.05(+0)	7.50(+0)	2.00(+1)	9.00(+1)	; $\lambda_0^{(5)}(r) = 90\mathrm{e}^{r/37.5}$
T_i	2.73(+0)	9.92(+4)	1.37(+4)	1.92(+3)	7.19(+2)	1.60(+2)	; $T_5(r) = 160\mathrm{e}^{-r/37.5}$
σ_i	———	3.39(−1)	6.10(−1)	2.20(−1)	2.19(−1)	4.72(−1)	; $\sigma_2(r) = 0.61\mathrm{e}^{r/87.0}$
$\epsilon_{\rm ph,0}^{(i)}$	2.61(−1)	5.20(−1)	7.92(+0)	8.10(−1)	3.40(−1)	4.10(+0)	; $\epsilon_{\rm ph}^{(i)}(r) = \epsilon_{\rm ph,0}^{(i)}\mathrm{e}^{-r/3.2}$
$\epsilon_{\rm ph}^{(i)}$	2.61(−1)	2.03(−1)	1.39(+1)	3.17(−1)	1.33(−1)	1.61(+0)	; $\epsilon_{\rm ph}^{(2)}(r) = 13.9\mathrm{e}^{-r/2.0}$

Table 4. Summary of parameters often appearing in our propagation model, classifying them into two groups, one related to the gas density of ISM, $\bar{n}(\boldsymbol{r})$, and another to the energy density of ISRF, $\bar{\epsilon}(\boldsymbol{r})$.

Parameters for ISM	Typical values for ISM	Parameters for ISRF	Typical values for ISRF
$\nu = \dfrac{1}{1 + z_D/z_n}$	$\nu = 0.04 - 0.06$	$\kappa = \dfrac{1}{1 + z_D/z_\epsilon}$	$\kappa = 0.15 - 0.21$
$U_\nu = 2\sqrt{\nu + \nu^2}$	$U_\nu = 0.4 - 0.5$	$U_\kappa = 2\sqrt{\kappa + \kappa^2}$	$U_\kappa = 0.8 - 1.2$
$\dfrac{1}{\bar{r}_n} = \dfrac{1}{2}\left(\dfrac{1}{r_D} + \dfrac{1}{r_n}\right)$	$\bar{r}_n = [20 - 40]$kpc	$\dfrac{1}{\bar{r}_\epsilon} = \dfrac{1}{2}\left(\dfrac{1}{r_D} + \dfrac{1}{r_\epsilon}\right)$	$\bar{r}_\epsilon = [5 - 10]$kpc
$\dfrac{1}{\bar{z}_n} = \dfrac{1}{2}\left(\dfrac{1}{z_D} + \dfrac{1}{z_n}\right)$	$\bar{z}_n = [0.3 - 0.5]$kpc	$\dfrac{1}{\bar{z}_\epsilon} = \dfrac{1}{2}\left(\dfrac{1}{z_D} + \dfrac{1}{z_\epsilon}\right)$	$\bar{z}_\epsilon = [1.0 - 1.4]$kpc
$\omega_\nu = \left(\dfrac{1}{z_Q} - \dfrac{1}{2z_n}\right)\bar{z}_n$	$\omega_\nu = 0.8 - 1.2$	$\omega_\kappa = \left(\dfrac{1}{z_Q} - \dfrac{1}{2z_\epsilon}\right)\bar{z}_\epsilon$	$\omega_\kappa = 4.5 - 5.5$

so that in the following discussion, we give first the solution of the diffusion equation (21) in the HE region, regarding $\bar{n}\mathcal{W}_n$ as a perturbative term, where we can neglect the fluctuation term due to the reacceleration. Next we give the solution in the LE region, regarding $\bar{\epsilon}\mathcal{W}_\epsilon$ as a perturbative term by contrast, which is completely the same as the former one after replacing $[\bar{\epsilon}, \mathcal{W}_\epsilon]$ with $[\bar{n}, \mathcal{W}_n]$ (and vice versa), while we have to take the fluctuation term, $\langle \Delta E_e^2 \rangle_{\mathrm{rea}}$, into account in this case.

Thus for the steady state $(\partial/\partial t = 0)$, the solution of equation (21) in the HE region is devided into three

$$N_{e,\epsilon} \simeq N_{e,\epsilon}^{(0)} + \tilde{N}_{e,n}^{(0)} + N_{e,\epsilon}^{(1)}, \tag{26a}$$

where the first term is a principal one coming from $\bar{\epsilon}\mathcal{W}_\epsilon$, the second term corresponds to the perturbative term from $\bar{n}\mathcal{W}_n$, and the third term to the fluctuation due to the reacceleration given by the second term of the right-hand in equation (22), while it is negligible in practice, $N_{e,\epsilon}^{(1)} \approx 0$.

The solution in the LE region is similarly given by replacing the suffix ϵ with n (and vice versa), but we can not neglect the fluctuation term $N_{e,n}^{(1)}$ in contrast,

$$N_{e,n} \simeq N_{e,n}^{(0)} + \tilde{N}_{e,\epsilon}^{(0)} + N_{e,n}^{(1)}. \tag{26b}$$

The first term in equation (26a) is written immediately as

$$N_{e,\epsilon}^{(0)}(\boldsymbol{r}; E_e) = \int_0^\infty \Pi_\epsilon^{(0)}(\boldsymbol{r}; y) f_\epsilon^{(0)}(y; E_e) dy, \tag{27}$$

where $\Pi_\epsilon^{(0)}$ and $f_\epsilon^{(0)}$ satisfy,

$$\left[\bar{\epsilon}(\boldsymbol{r}) c \frac{\partial}{\partial y} - \nabla \cdot D(\boldsymbol{r}) \nabla \right] \cdot \Pi_\epsilon^{(0)}(\boldsymbol{r}; y) = Q(\boldsymbol{r}) \delta(y), \tag{28a}$$

$$\left[c E_e^\alpha \frac{\partial}{\partial y} - \frac{\partial}{\partial E_e} \mathcal{W}_\epsilon(E_e) \right] \cdot f_\epsilon^{(0)}(y; E_e) = 0, \tag{28b}$$

with $f_\epsilon^{(0)}(0; E_e) = E_e^{-\gamma-\alpha}$.

4.2. Solution in the steady state

It is possible to solve exactly equation (28a) with use of the procedure presented in Paper I, after replacing $\bar{n}(\boldsymbol{r})$ by $\bar{\epsilon}(\boldsymbol{r})$, and we present here only the critical term related to $(r, z; y)$, omitting constant terms such as Q_0 and $\bar{\epsilon}_0$ (see Appendix B for the full form),

$$\Pi_\epsilon^{(0)}(\boldsymbol{r}; y) \propto \exp[-\bar{s}_r y - |z|/z_D], \tag{29}$$

$$\bar{s}_r \simeq \frac{D_r}{\bar{\epsilon}_r c z_D^2}\left(1 + \frac{1}{\kappa}\right); \quad \kappa = \frac{1}{1 + z_D/z_\epsilon}, \tag{30}$$

with $D_r \equiv D(r, 0)$, $\bar{\epsilon}_r \equiv \bar{\epsilon}(r, 0)$. As $\Pi_\epsilon^{(0)}$ is of the form of $\mathrm{e}^{-\bar{s}_r y}$, the Laplace transform of $f_\epsilon^{(0)}$ with respect to y, $F_{r,\epsilon}^{(0)}(E_e)$, is sufficient for our purpose to obtain the electron density,

$$F_{r,\epsilon}^{(0)}(E_e) = \int_0^\infty \mathrm{e}^{-\bar{s}_r y} f_\epsilon^{(0)}(y; E_e)dy,$$

thus we have immediately from equation (28b)

$$F_{r,\epsilon}^{(0)}(E_e) = \frac{c}{\mathcal{W}_\epsilon(E_e)}\int_{E_e}^\infty dE_0 E_0^{-\gamma}\mathrm{e}^{-Y_{r,\epsilon}(E_e, E_0)}, \tag{31}$$

with

$$Y_{r,\epsilon}(E_e, E_0) = c\bar{s}_r \int_{E_e}^{E_0}\frac{E^\alpha}{\mathcal{W}_\epsilon(E)}dE.$$

In the HE limit, $E_e \gg 1\,\mathrm{GeV}$, using equation (18b), we find

$$F_{r,\epsilon}^{(0)}(E_e) \simeq \frac{cE_e^{-(\gamma+1-\delta)}}{(1-\alpha-\delta)w_\mathrm{T}}\left[1 - \frac{\gamma+\alpha-\delta-2}{c\bar{s}_r E_e^\alpha/w_\mathrm{T}} + \dots\right],$$

giving a spectral index with $\gamma + 1 - \delta$, where $\delta\,(= 0.075)$ comes from the effect of the Klein-Nishina cross-section. Practically, however, it must be softer than the above index because of the exponential cutoff with $\mathrm{e}^{-E_e/E_\mathrm{cut}}$ in the electron injection spectrum somewhere around $20\,\mathrm{TeV}$ (Reynolds & Keohane 1999; Hendrick & Reynolds 2001; Yamazaki et al. 2006).

Now the principal term, $N_{e,\epsilon}^{(0)}$, in equation (26a) for the electron density in the HE region, $E_e \gtrsim E_c^+$, is given by

$$N_{e,\epsilon}^{(0)}(\boldsymbol{r}; E_e) \propto F_{r,\epsilon}^{(0)}(E_e)\,\mathrm{e}^{-|z|/z_D}, \tag{32}$$

while the perturbative term, $\tilde{N}_{e,n}^{(0)}$, is obtained by the use of the iteration method as presented in Appendix B1, giving $\tilde{N}_{e,n}^{(0)}/N_{e,\epsilon}^{(0)} \sim 10\%$ with the first iteration for $E_e \gtrsim 1\,\mathrm{GeV}$ at SS as shown in Figure 24a. In practice, we perform only the first iteration, neglecting the second and higher iterations. Full form of $N_{e,\epsilon}(\boldsymbol{r}; E_e)$ is given by equation (B3).

The numerical procedure in the LE region is similar to that in the HE region mentioned above by replacing the suffix "ϵ" with "n" (and vice versa), while we have to take into account the third term in equation (26b), $N_{e,n}^{(1)}$, corresponding to the fluctuation. We find again that the perturbative term, $\tilde{N}_{e,\epsilon}^{(0)}$, is obtained by the use of the iteration method as presented in Appendix B2, giving $\tilde{N}_{e,\epsilon}^{(0)}/N_{e,n}^{(0)} \sim 10\%$ with the first iteration for $E_e \lesssim 10\,\mathrm{GeV}$, as shown in Figure 24b.
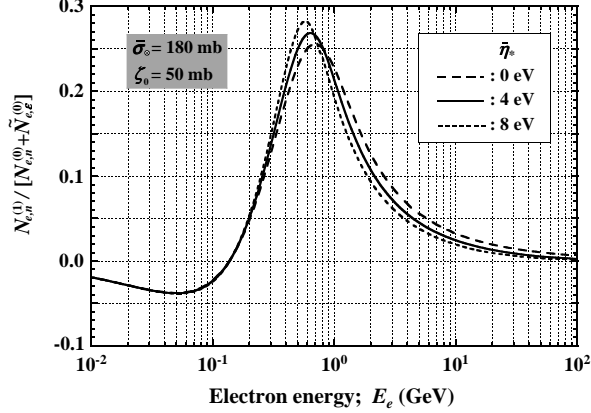
Fig. 7.— Contributions of the fluctuation in the reacceleration with $[\bar{\sigma}_\odot, \zeta_0] = [180, 50]$ mbarn at SS for several sets of the free parameter $\bar{\eta}_*$ given by equation (B6).

On the other hand, the numerical procedure in the fluctuation effect due to the reacceleration is a little bit cumbersome, which is presented in Appendix B3. We give an example of the ratio, $N_{e,n}^{(1)}/[N_{e,n}^{(0)} + \tilde{N}_{e,\epsilon}^{(0)}]$, at SS for the first iteration in Figure 7, where $\bar{\eta}_*$ is the *effective* ratio of the energy density to the gas density defined by equation (B6), approximately with 2eV. One finds that it is significant around 0.3–1.5 GeV in the case of $\zeta_0 = 50$ mbarn, boosting the solution without the fluctuation, $N_{e,n}^{(0)} + \tilde{N}_{e,\epsilon}^{(0)}$, by approximately 25%. So we perform only the first iteration also for $N_{e,n}^{(1)}$ in the LE region, as the contribution coming from the second and higher iterations is at most of the magnitude of a few % or less (Ishikawa 2010). Full form of $N_{e,n}(\boldsymbol{r}; E_e)$ is given by equation (B15).

Finally, we give the electron density covering all energies so that it continues smoothly at the energy E_c between the HE and LE regions at the SS ($\boldsymbol{r} = \boldsymbol{r}_\odot$), with $E_c \approx E_c^+$ in practice, but not always $E_c = E_c^+$,

$$
\frac{N_e(\boldsymbol{r}; E_e)}{N_{e,0}} = \begin{cases} \dfrac{F_{r,\epsilon}(E_e)}{F_{\odot,\epsilon}(E_c)} \mathrm{e}^{-|z|/z_D} : & \text{for } E_e \geq E_c, & \text{(33a)} \\[3mm] \dfrac{F_{r,n}(E_e)}{F_{\odot,n}(E_c)} \mathrm{e}^{-|z|/z_D} : & \text{for } E_e \leq E_c, & \text{(33b)} \end{cases}
$$

with

$$
\frac{\partial}{\partial E_e} \frac{F_{\odot,\epsilon}(E_e)}{F_{\odot,\epsilon}(E_c)}\bigg|_{E_e=E_c} = \frac{\partial}{\partial E_e} \frac{F_{\odot,n}(E_e)}{F_{\odot,n}(E_c)}\bigg|_{E_e=E_c},
$$

see equations (B4) and (B13) for $F_{r,\epsilon}(E_e)$ and $F_{r,n}(E_e)$ respectively, and $N_{e,0}$ is determined by the normalization with the experimental data as discussed in §5.

4.3. Numerical results

In Figure 8 we show the numerical results of $N_e(\boldsymbol{r}_\odot; E_e)/N_{e,0}$ in two cases, (a) $[\zeta_0, \bar{\sigma}_\odot, \bar{s}_\odot] = [50, 180, 30\,\mathrm{eV}^{-1}]$mbarn with $\alpha = \frac{1}{3}$ (reacceleration with Kolmogorov-type spectrum in hydromagnetic turbulence), and (b) $[0, 90, 15\,\mathrm{eV}^{-1}]$mbarn with $\alpha = \frac{1}{2}$ (no reacceleration with Kraichnan-type spectrum) for $\bar{\epsilon}_\odot/\bar{n}_\odot = 2\,\mathrm{eV}$ with $\beta\ (\equiv \gamma + \alpha) = 2.6$, 2.7 and 2.8, see equation (30) with $r = r_\odot$ for $\bar{s}_\odot$, where we assume $E_{\mathrm{cut}} = 20\,\mathrm{TeV}$ (Reynolds & Keohane 1999; Hendrick & Reynolds 2001; Yamazaki et al. 2006) in the electron injection spectrum with $E_e^{-\gamma}\mathrm{e}^{-E_e/E_{\mathrm{cut}}}$, and the results show the use of both Klein-Nishina (*solid curves*) and Thomson (*dotted curves*) cross-sections.

We find two critical points in Figure 8. First, those by the former cross-section give approximately 40–50% (20–30%) larger than those by the latter at $1\,\mathrm{TeV}$ ($100\,\mathrm{GeV}$), where the density is normalized at $E_e = 10\,\mathrm{GeV}$, leading to significantly harder spectra than those with the Thomson cross-section, as expected. Similar results are also recently reported by Delahaye et al. (2010), while their main purpose is to study the nearby sources of electron and the positron excess problem as well, which are outside the range of the present paper.

Second, the reacceleration effect is significant in the energy region less than $10\,\mathrm{GeV}$ as compared to the curves without the reacceleration process. Unfortunately, however, it is difficult to observe such a signal in the *direct* experimental data on the electron component
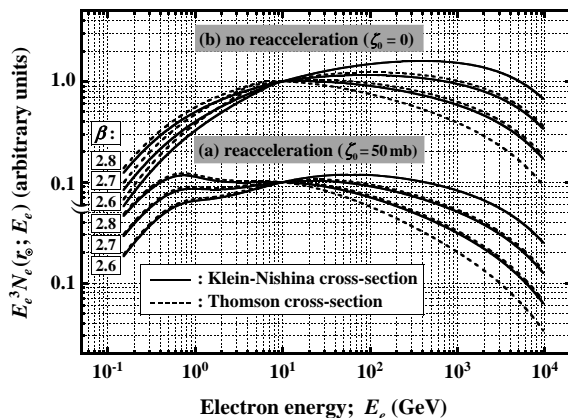

Fig. 8.— Numerical results of the electron density, $N_e(r_\odot; E_e)$, at the SS ($r = r_\odot$) in the case of (a) reacceleration with $[\alpha; \zeta_0, \bar{\sigma}_\odot] = [\frac{1}{3}; 50\,\mathrm{mbarn}, 180\,\mathrm{mbarn}]$, and (b) no reacceleration with $[\frac{1}{2}; 0, 90\,\mathrm{mbarn}]$, for $\beta = 2.6$, 2.7, and 2.8, where the vertical axis is multiplied by E_e^3, and normalized to $E_e = 10\,\mathrm{GeV}$. We show results for two cross-sections in IC process from the Thomson (*dotted curves*) and Klein-Nishina (*solid curves*) formulae.
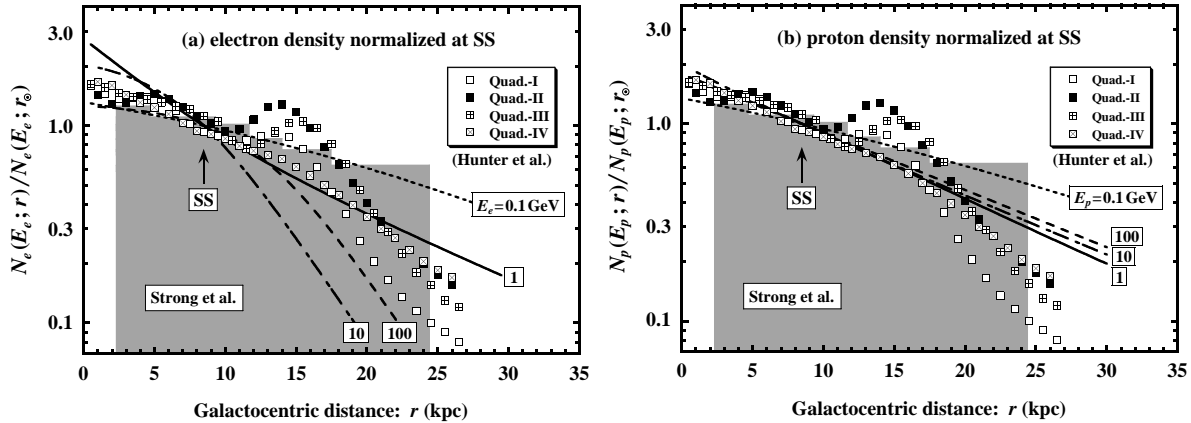
Fig. 9.— CR densities of (a) electrons, $N_e(r; E_e)$, and (b) protons, $N_p(r; E_p)$, as a function of the galactocentric distance r for several energies, where the vertical axis is normalized to the density at SS ($r = r_\odot$). We present also those given by Hunter et al. (1997) (four kinds of *square symbols*), and by Strong et al. (1988) (*thin filled histograms*), where the CR densities are averaged azimuthally in each galactocentric quadrant by Hunter et al. (1997), assuming that they are coupled to the gas density of ISM independent of the energy, while azimuthal symmetric γ-ray emissivity is used by Strong et al. (1988).

because of the modulation effect in the low energy region $\lesssim 5\,\text{GeV}$, which masks the electron flux boosted by the reacceleration, see Figure 13, even if it occurs actually.

Next we examine the spatial dependence of the electron density. First it attenuates exponentially with the latitudinal distance z from the GP with the latitudinal scale height of the diffusion coefficient, $z_D = 2$–$4\,\text{kpc}$, independent of the energy E_e. This is the same result as in the case of the proton density, $N_p(\boldsymbol{r}; E_p)$ (Paper V), namely the ratio of electron density to the proton density is independent of z.

Contrary to the latitudinal behavior, the longitudinal behavior of the CR densities, $N_e(\boldsymbol{r}; E_e)$ and $N_p(\boldsymbol{r}; E_p)$, are somewhat complicated, both of which depend on the energy, and appear implicitly in the form of $\bar{s}_r$ and $\bar{\sigma}_r$ (see Paper I for $\bar{\sigma}_r$ and its physical meaning). We present these in Figure 9 against the radial distance r for the (a) electron and (b) proton components, both normalized at the SS for four energies, 0.1, 1, 10, and $100\,\text{GeV}$, with $\beta = 2.7$, where the scale heights are set as $[\bar{r}_n, \bar{r}_\epsilon] = [30,\ 8]\,\text{kpc}$ and $[z_D; z_n, z_\epsilon] = [3;\ 0.2,\ 0.75]\,\text{kpc}$ (see Table 4 for $\bar{r}_n$ and $\bar{r}_\epsilon$). We plot the results of Hunter et al. (1997; *square symbols*) and Strong et al. (1988; *thin filled histogram*) together, where the former are based on the assumption that the CR density is coupled to the density of ISM, and plotted separately for four galactocentric quadrants, I, II, III, and IV. We find that the radial dependence of the electron density, $N_e(\boldsymbol{r}; E_e)$, is much stronger than that of the proton density, $N_p(\boldsymbol{r}; E_p)$, in

the energy region of 1–100 GeV as expected, while the other two authors assume no spatial dependence in the energy spectrum, namely the *shape* of the energy spectrum at the SS is the same everywhere in the Galaxy.

5. Electron-induced γ-ray spectrum

For convenience in the following discussion, we summarize two cross-sections in Table 5, $\sigma_{\mathrm{EB}}(E_e, E_\gamma)$ and $\sigma_{\mathrm{IC}}(E_e, E_\gamma; E_{\mathrm{ph}})$, each for the bremsstrahlung (abbreviated as "EB" for subscript attached here and in the following) and the IC processes respectively, where E_{ph} is the energy of target photon before scattering. In these cross-sections, we take into account the screening effect for the bremsstrahlung (Koch & Motz 1959; Gould 1969), and the Klein-Nishina cross-section (Jones 1965, 1968; Blumenthal & Gould 1970) for IC. In the following discussion, we put $F_r(E_e) \equiv F_{r,\epsilon}(E_e)$ for $E_e \geq E_c$, and $F_r(E_e) \equiv F_{r,n}(E_e)$ for $E_e \leq E_c$ in equation (33) for simplicity.

First we consider the emissivity of γ's from the bremsstrahlung at the position $\boldsymbol{r}$, which is immediately written down as

$$q_{\mathrm{EB}}(\boldsymbol{r}; E_\gamma) = \int_{E_\gamma}^\infty N_e(\boldsymbol{r}; E_e)[n(\boldsymbol{r})c\sigma_{\mathrm{EB}}(E_e, E_\gamma)]dE_e, \tag{34}$$

where the electron density, $N_e(\boldsymbol{r}; E_e)$, is given by equation (33). For the numerical calculation of equation (34), we need the *absolute* electron density at $\boldsymbol{r}$. To do so, we use the observational data on the electron intensity at the SS, $dI_e^\odot/dE_e$, which is related to the electron density by

$$\frac{dI_e^\odot}{dE_e}(E_e) = \frac{c}{4\pi} N_e(\boldsymbol{r}_\odot; E_e).$$

In practice, we normalize the electron density at $E_s = 10\,\mathrm{GeV}$ with use of the most recent data (see Fig. 14), where the solar modulation effect is negligible,

$$cN_s^\odot \equiv cN_e(\boldsymbol{r}_\odot; E_s) = 2.26\,\mathrm{m}^{-2}\mathrm{s}^{-1}\mathrm{GeV}^{-1},$$

corresponding to $dI_e^\odot/dE_e = 0.180\,\mathrm{m}^{-2}\mathrm{sr}^{-1}\mathrm{s}^{-1}\,\mathrm{GeV}^{-1}$ at $E_e = 10\,\mathrm{GeV}$ in Figure 14, while $E_s = 100$ GeV (per nucleon) for the hadron-induced γ's ($\pi^0 \rightarrow 2\gamma$) with $cN_p(\boldsymbol{r}_\odot; E_s) = 6.16\,\mathrm{m}^{-2}\mathrm{s}^{-1}\mathrm{GeV}^{-1}$ (Paper V). One should keep in mind that the uncertainty in the normalization is of the magnitude as large as 10%.

Table 5. Summary of the production cross-sections of γ-rays in the bremsstrahlung and the IC processes with $x = E_\gamma/E_e$, where E_e is the incident energy of electron, and E_γ is the energy of the produced γ's, and $E_{\rm ph}$ the energy of the target photon before electron scattering. For the bremsstrahlung process, we present the cross-section in the case of only one-electron atoms ($Z = 1$), see Gould (1969) for two-electron atoms ($Z = 2$).

bremsstrahlung (EB)	inverse Compton (IC)
$\sigma_{\rm EB}(E_e, E_\gamma)dE_\gamma = \sigma_{\rm EB}^{(0)}\, \phi_{\rm EB}(x, E_\gamma)\dfrac{dx}{x}$	$\sigma_{\rm IC}(E_e, E_\gamma; E_{\rm ph})dE_\gamma = \sigma_{\rm IC}^{(0)}\, \phi_{\rm IC}(x, q)\dfrac{dx}{X}$
$\sigma_{\rm EB}^{(0)} = 4\alpha_f Z(Z+1)\left(\dfrac{e^2}{m_e c^2}\right)^2; \quad \alpha_f = \dfrac{1}{137}$	$\sigma_{\rm IC}^{(0)} = 3\sigma_{\rm T} = 8\pi\left(\dfrac{e^2}{m_e c^2}\right)^2$
$\phi_{\rm EB}(x, E_\gamma) = \left\{1 + (1-x)^2\right\}\phi_1(\chi) - \dfrac{2}{3}(1-x)\phi_2(\chi)$	$\phi_{\rm IC}(x, q) = 2q \ln q + (1-q)\left(1 + 2q + \dfrac{1}{2}\dfrac{x^2}{1+x}\right)$
$\phi_1(\chi) = 1 + \displaystyle\int_\chi^1 \phi_0(y)\left(1 - \dfrac{\chi}{y}\right)^2\dfrac{dy}{y}$	$q \equiv q(x, X) = \dfrac{x}{1-x}\dfrac{1}{X}$
$\phi_2(\chi) = \dfrac{5}{6} + \displaystyle\int_\chi^1 \phi_0(y)\left\{1 + 3\dfrac{\chi^2}{y^2}\left(1 + \ln\dfrac{\chi^2}{y^2}\right) - 4\dfrac{\chi^3}{y^3}\right\}\dfrac{dy}{y}$	$X \equiv X(E_e, E_{\rm ph}) = \dfrac{k}{\Theta_e^2} = \dfrac{E_{\rm ph}E_e}{[m_e c^2/2]^2}$
$\phi_0(y) = 1 - \dfrac{1}{[1 + y^2/(2\alpha_f Z)^2]^2}$	$k \equiv k(E_{\rm ph}, T_{\rm ph}) = \dfrac{E_{\rm ph}}{k_{\rm B}T_{\rm ph}}$
$\chi \equiv \chi(x, E_\gamma) = \dfrac{x^2}{1-x}\dfrac{m_e c^2}{2E_\gamma}$	$\Theta_e \equiv \Theta_e(E_e, T_{\rm ph}) = \dfrac{m_e c^2/2}{\sqrt{k_{\rm B}T_{\rm ph}E_e}}$

Thus taking care of the terms related to $\boldsymbol{r}$, we have

$$\frac{q_{\mathrm{EB}}(\boldsymbol{r}; E_\gamma)}{n(\boldsymbol{r})w_{\mathrm{EB}}^{(0)}N_s^\odot} = \mathrm{e}^{-|z|/z_D}\int_0^1 \phi_{\mathrm{EB}}(x, E_\gamma)\frac{F_r(E_x)}{F_\odot(E_s)}\frac{dx}{x^2}, \tag{35}$$

for $E_\gamma \geq E_c$ with $E_x = E_\gamma/x$, and $w_{\mathrm{EB}}^{(0)} = c\sigma_{\mathrm{EB}}^{(0)} = 1.39{\times}10^{-16}\mathrm{cm}^3\mathrm{s}^{-1}$ for the hydrogen gas ($Z = 1$), where one should take care of the energy range $E_e \leq E_c$ in the case of $E_\gamma \leq E_c$.

Next we consider the emissivity of γ's coming from the IC process, which is somewhat complicated, as there are several kinds of target photons with different energy density as well as with different scale heights in the spatial gradient. Here we present a result only, taking into account the six wavelength bands in $\epsilon_{\mathrm{ph}}^{(i)}(\boldsymbol{r})$ ($i = 0$–5) (see eq. [7] and Table 3),

$$\frac{q_{\mathrm{IC}}^{(i)}(\boldsymbol{r}; E_\gamma)}{\epsilon_{\mathrm{ph}}^{(i)}(\boldsymbol{r})w_{\mathrm{T}}N_s^\odot} = \mathrm{e}^{-|z|/z_D}\int_0^1 \Phi_{\mathrm{IC}}^{(i)}(x, E_\gamma)\frac{F_r(E_x)}{F_\odot(E_s)}\frac{dx}{x^2}, \tag{36}$$

where $\Phi_{\mathrm{IC}}^{(i)}(x, E_\gamma)$ is given by equation (C2), see Appendix C for the details.

Let us show the numerical results for two cases of emissivity in Figure 10, (a) $r/r_\odot = 0.5, 1, 2$ with $z = 0$ in the GP, and (b) $z = 0.2, 0.4, 0.6\,\mathrm{kpc}$ with $r = r_\odot$ normal to the GP at SS, assuming $\beta \equiv \gamma + \alpha = 2.7$, where we present separately those coming from π^0 (solid curves), EB (broken curves), and IC (dotted curves). One finds that EB-γ's and π^0-γ's are comparable around $50\,\mathrm{MeV}$, and IC-γ's and π^0-γ's around two energies, $\sim 20\,\mathrm{MeV}$ and $\sim 1\,\mathrm{TeV}$.

See Paper V for the emissivity originating in π^0, $q_{\pi^0}(\boldsymbol{r}; E_\gamma)$, while we use more realistic gas density, $n(\boldsymbol{r})$, in the present paper. Note also in q_{π^0} that the semi-empirical production cross-section of γ's, $\sigma_{pp\to\gamma}(E_p, E_\gamma)$, in proton-proton collision we use is valid over very wide energy ranges, $1\,\mathrm{GeV}$–$1\,\mathrm{PeV}$, reproducing nicely various kinds of physical quantities such as psuedo-rapidity, energy spectrum, multiplicity, etc, obtained by both the accelerator and CR experiments with local target layer (Suzuki, Watanabe & Shibata 2005).

Once we have the emissivity of γ's induced by the interaction between the electrons and the media of ISM and ISRF, we can obtain immediately the intensity of γ's observed at the SS ($\boldsymbol{r} = \boldsymbol{r}_\odot$), coming from the direction $\boldsymbol{\theta}(l, b)$

$$\frac{d^3 I_\gamma^\odot(\boldsymbol{\theta}; E_\gamma)}{dE_\gamma dl d(\sin b)} = \frac{1}{4\pi}\int_0^\infty q_\gamma(\boldsymbol{r}; E_\gamma)ds,$$

with

$$q_\gamma(\boldsymbol{r}; E_\gamma) = q_{\mathrm{EB}}(\boldsymbol{r}; E_\gamma) + \sum_{i=0}^5 q_{\mathrm{IC}}^{(i)}(\boldsymbol{r}; E_\gamma),$$
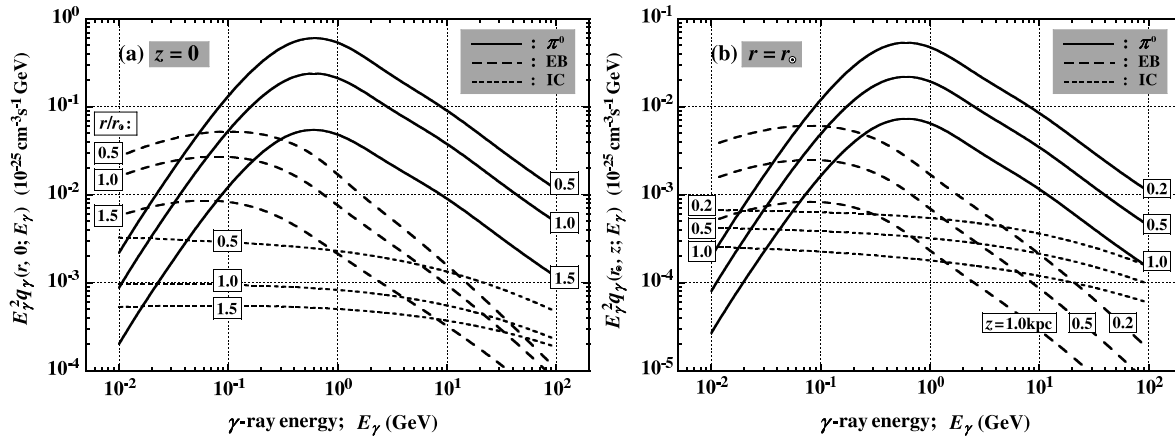
Fig. 10.— Emissivity of γ's (a) at three radial distances, $r/r_\odot = 0.5$, 1.0, 1.5 in the galactic plane ($z = 0$), and (b) at three latitudinal distances, $z = 0.2$, 0.4, 0.6 kpc with $r = r_\odot$, where the three components for γ's emission, π^0 (*solid curves*), EB (*broken curves*), and IC (*dotted curves*) are shown separately.

where the integration with respect to s is performed along the arrival direction of γ's, $\boldsymbol{\theta}(l, b)$, at the SS, and $\boldsymbol{r}(r, z)$ is bound to $(s; l, b)$ as follows,

$$r(s;\, l, b) = \sqrt{r_\odot^2 + s^2 \cos^2 b - 2r_\odot s \cos b \cos l},$$

$$z(s;\, b) = s \sin b.$$

6. Comparison with the observational data

6.1. Critical parameters

We assume that the source distribution of electron component, $Q(\boldsymbol{r}; E_e)$, is the same as that of the hadronic component except for the cutoff electron energy, for instance $E_{\rm cut} \approx 20\,\mathrm{TeV}$, with the supernova remnants as the main energy supply, while the pulsars and pulsar wind nebulae might contribute to them as well, particularly to positrons and electrons (for instance, Delahaye et al. 2010). So the galactic parameters used in the present work are essentially the same as those appearing in Papers I–V, and we summarize them briefly in the following.

The recent observational data on the energy spactra of CR hadronic components give indices with 2.74 ± 0.08 for proton (Derbina et al. 2005), and with a common value of $\sim$2.7 for nuclei between the oxygen and iron (Müller 2009), whereas there still remains uncertainty

for helium, for instance with 2.68 ± 0.05 by JACEE (Asakimori et al. 1998) in contrast to 2.78 ± 0.20 by RUNJOB (Derbina et al. 2005). Note that PAMELA (Picozza et al. 2007) reports recently a common index of 2.73 in both the proton and helium spectra, albeit the energy region is limited below $500\,\mathrm{GeV}$. Any way, the spectrum index β of proton, must lie well within 2.7–2.8 in the high energy region at the SS, which is the most effective element for the hadron-induced Dγ's. See Paper V for the contribution of helium and nuclei to Dγ's, which is taken into account by introducing the enhancement factor with 1.53. So in the present paper we use the critical parameter β in place of γ (source index of the energy spectrum) with $\beta = \gamma + \alpha$, and consider three values of β; 2.6, 2.7, and 2.8, each for $\alpha = \frac{1}{3}$ (Kolmogoroph-type spectrum) and $\frac{1}{2}$ (Kraichnan-type spectrum).

There are three galactic parameters, $[D(\boldsymbol{r}),\ \bar{n}(\boldsymbol{r}),\ Q(\boldsymbol{r})]$, in our approach to the CR propagation, and six scale heights for longitudinal and latitudibal directions correspoding to each one, $[r_D, r_n, r_Q]$ and $[z_D, z_n, z_Q]$, respectively. In practice, however, explicit parameters needed to compare with the experimental data appear in two critical ones alone, $\bar{\sigma}_r$ and ζ_0, besides $[\alpha,\ \beta]$ mentioned above, while the parameter, $\bar{\mu}_r \equiv 2z_D/\sqrt{\bar{\tau}_0 D_r}$, is also important for the study of the CR isotopes ($\bar{\tau}_0$: normalized life time of an isotope with 10^6yr).

For electron components, the additional parameter newly appears, $\bar{s}_r$, given by equation (30), physical meaning of which is essentially the same as $\bar{\sigma}_r$; i.e., while the inverse of $\bar{\sigma}_r$ gives the average path length, $\bar{x}_r$, in units of cm^{-2} in ISM as discussed in Paper I, that of $\bar{s}_r$ corresponds to the average path length, $\bar{y}_r$, in units of eVcm^{-2} in ISRF, namely the total amount of photon-gas energy that CR has passed through the ISRF.

Now from equation (33), one should remark that there appear only *three* critical parameters, $[\zeta_0,\ \bar{\sigma}_\odot,\ \bar{s}_\odot]$, in $F_{r,\epsilon}(E_e)$ and $F_{r,n}(E_e)$ needed to compare with the observational data, aside from two critical indices, $[\alpha,\ \beta]$, note that various galactic parameters such as the diffusion constant, gas density, energy density, their scale heights, etc are all involved implicitly in these three ones.

6.2. Charged components

6.2.1. Hadron components

As we have presented the experimental results on CR hadron components in the past papers (Papers I–IV), we give here only three kinds of secondary-to-primary ratio with new data, B/C, sub-Fe/Fe, and $\bar{p}/p$, that have since become available. See Paper III for the secondary unstable nuclei, while new data are still not available.

In Figure 11, we present B/C and sub-Fe/Fe, plotted together with new ones from CREAM (Ahn et al. 2008) and TRACER (Müller 2009), where we plot also RUNJOB (Derbina et al. 2005) data for reference, while the data quality is rather poor with large
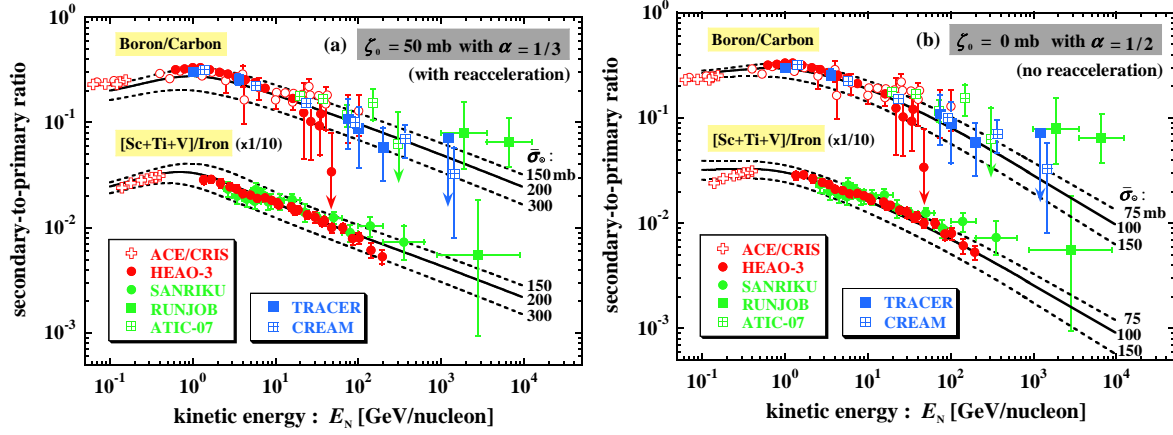

Fig. 11.— Energy dependence of the secondary-to-primary ratio for boron/carbon and sub-iron/iron. See Paper II and references therein for the experimental data, while CREAM (Ahn et al. 2008) and TRACER (Müller 2009) data are newly plotted. Numerical curves are demonstrated for two cases; (a) reacceleration with $(\alpha, \zeta_0) = (\frac{1}{3}, 50\,\text{mbarn})$ and (b) no reacceleration with $(\frac{1}{2}, 0)$.
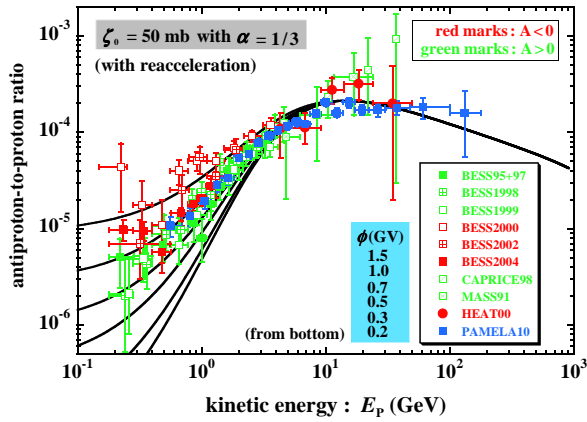
Fig. 12.— Energy dependence of the antiproton-to-proton ratio, where we assume the reacceleration model with $\alpha = \frac{1}{3}$ for six modulation parameters, 0.2, 0.3, 0.5, 0.7, 1.0, and 1.5 GV, and $A < 0$ ($A > 0$) corresponds to positive (negative) polarity state in heliospheric magnetic field, although the present calculations do not take the effect into account. See Paper IV and the references therein for the data other than PAMELA (Adriani et al. 2010).
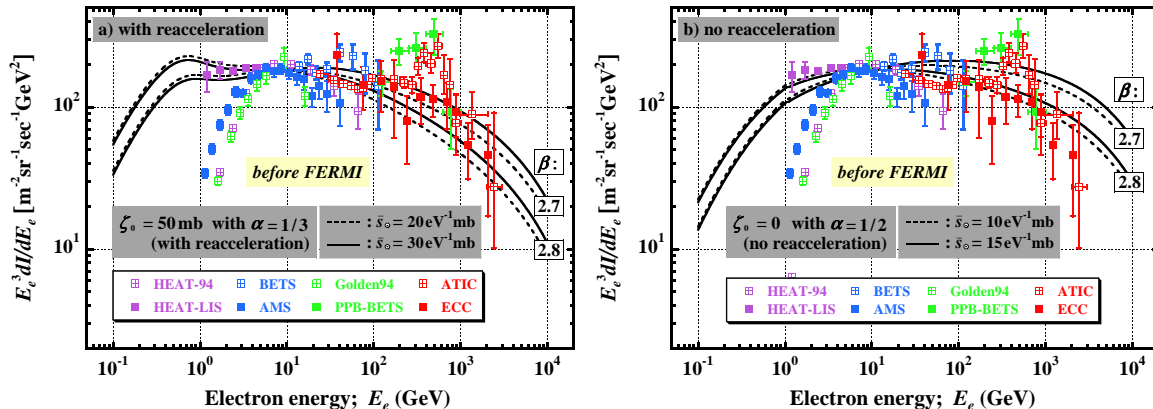
Fig. 13.— Electron energy spectra in two models, (a) with reacceleration and (b) no reacceleration, compared with the measurements, where the vertical axis is multiplied by E_e^3. All numerical values are normalized to $E_e = 10\,\mathrm{GeV}$, and several sets of $(\beta, \bar{s}_r)$ are assumed. See text for references for individual experimental data.

atmospheric correction. We compare our numerical results with the data for two models, (a) reacceleration with the set of $[\zeta_0, \bar{\sigma}_\odot] = [50, 150\text{–}300]$ mbarn, for $\alpha = \frac{1}{3}$, and (b) no reacceleration with $[0, 75\text{–}150]$ mbarn, for $\alpha = \frac{1}{2}$. It is still not clear which model reproduces the experimental data more satisfactorily. As is well known, the advantage of the former explains naturally the drop of the ratio in the lower energy region around ACE/CRIS (Davis et al. 2000) without assuming an ad hoc drop in the path length distribution.

Next we present $\bar{p}/p$ in Figure 12, plotted together with new data from PAMELA (Adriani et al. 2010), where we present numerical curves with several sets of modulation parameters, 0.2-1.5 GV, for the reacceleration model shown in Figure 11a. One finds that our result is in good agreement with the PAMELA in the high energy region around 100 GeV, where the modulation effect is absolutely negligible.

6.2.2. Electron component

Let us present the electron data separately before and after FERMI, where "electron" denotes both electron and positron. First in Figure 13 we present the electron energy spectrum before FERMI, where the experimental data are presented for those reported in the period from 1994 to 2008 alone (Golden et al. 1994; Kobayashi et al. 1999; DuVernois et al. 2001; Torii et al. 2001, 2006; Aguilar et al. 2002; Chang et al. 2008), and also plotted are the data (*filled purple squares*) for reference after applying a demodulated correction to

HEAT data, HEAT-LIS, (DuVernois et al. 2001) using the force-field approximation with the modulation parameter of 755 MV (670 MV) for the 1994 (1995) data.

The numerical curves are normalized at 10 GeV with two indices, $\beta = 2.7$, 2.8, assuming two models, (a) reacceleration and (b) no reacceleration each with the same parameter sets as those used in Figure 11, while we assume additionally two cases of $\bar{s}_\odot$, [20, 30] mbarn for the reacceleration (a), and [10, 15] mbarn for no reacceleration (b). Aside from the prominent spectral features around 500 GeV appearing in ATIC (Chang et al. 2008) and PPB-BETS (Torii et al. 2006) data, our model with the reacceleration reproduces the data well in the higher energy region, $\gtrsim 10$ GeV, in Figure 13a, where the solar modulation effect is small. On the other hand, the model without reacceleration in Figure 13b is somewhat difficult to fit to the demodulated HEAT-LIS data.

Now, in Figure 14 we present the most recent data obtained by FERMI (Abdo et al. 2009, 2010b) and H.E.S.S. (Aharonian et al. 2009) together with those presented in Figure 13, where numerical curves are the same as shown in Figure 13a. We find that both FERMI and H.E.S.S. data do not exhibit the prominent bump around 500 GeV reported by ATIC and PPB-BETS, with both giving a spectrum falling with energy as E^{-3} up to 1 TeV, which is not inconsistent with emulsion chamber data (Kobayashi et al. 1999) within the statistical errors. Looking Figure 14, however, we find that FERMI and H.E.S.S. data seem to deviate systematically from numerical curves with an enhancement by 20–30% around 500 GeV, indicating still some additional local sources of high energy CR electrons, which will be discussed again in §7.
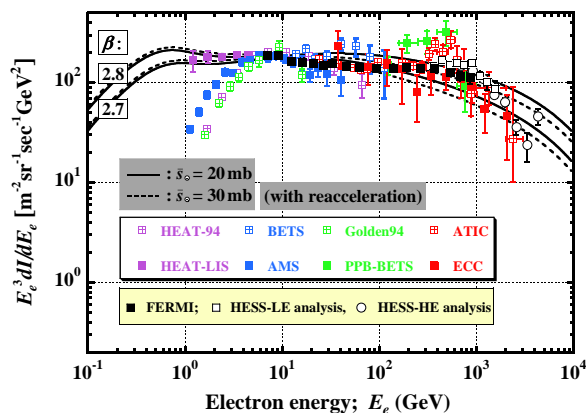

Fig. 14.— Same as Figure 13a, but with FERMI (Abdo et al. 2009, 2010b) and H.E.S.S. (Aharonian et al. 2009), where drawn are numerical curves with the reacceleration shown in Figure 13a.
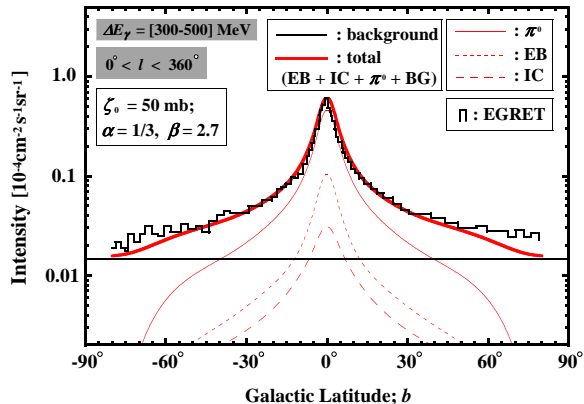
Fig. 15.—— An example of the estimation of the BG (*black horizontal line*) using the latitudinal Dγ's data from EGRET (Hunter et al. 1997) with the energy interval of 300–500 MeV averaged over the whole radial direction, $l = 0°$–$360°$.

6.3. Diffuse γ-ray component

6.3.1. Isotropic background γ-rays

Dγ's near the GP are mainly hadron-induced ($\pi^0 \to 2\gamma$) and electron-induced (EB + IC). In addition to these two components, we have isotropic background γ's (BGs) with various origins such as extragalactic sources (EGs), unidentified sources, instrumental sources, dark matter (DM), etc, so that the BGs depend on individual detectors with different sensitivity in energy and the angular resolution, while depending on the propagation model as well. Therefore it is not easy task to estimate the extragalactic Dγ, while its origin is one of the fundamental problems in astrophysics, studied in so many papers with various candidates; unresolved blazers (e.g. Stecker & Salamon 1996; Chiang & Mukherjee 1998; Mücke & Pohl 2000), intergalactic shocks produced by the assembly of large-scale structures (e.g. Loeb & Waxman 2000; Totani & Kitayama 2000; Miniati et al. 2000; Gabici & Blasi 2003), dark matter annihilation (e.g. Bergström 2000; Ullio et al. 2002; Ahn et al. 2007), etc. In the present paper, however, we use the acronym "BGs" all together for Dγ's other than those induced by π^0, EB (bremsstrahlung) and IC, while acknowledging EGRET and FERMI teams have estimated very carefully the EG-γ intensity.

In Figure 15, we present an example of EGRET data (*histogram*; source subtracted) (Hunter et al. 1997) together with numerical curves on the latitudinal distribution averaged over full longitude ranges, $0°$–$360°$ with the energy interval 300–500 MeV, where we give the contributions of Dγ's separately from π^0 (*solid red*), EB (*dotted red*), IC (*broken red*), BG (*solid black*), and total flux, π^0+EB+IC+BG (*heavy solid red*), assuming
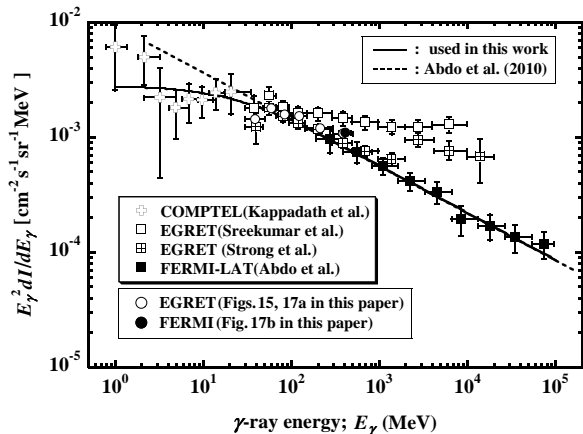
Fig. 16.— The BG spectrum obtained by COMPTEL (Kappadath et al. 1996), EGRET (Sreekumar et al. 1998), EGRET (revised; Strong et al. 2004), and FERMI (Abdo et al. 2010a), where also plotted are those estimated by the present work using EGRET and FERMI data (see Figs. 15 and 17). Dotted line is given by Abdo et al., and the solid curve is used in the present work (see text), modifying it slightly in the low energy region.

$[\zeta_0, \bar{\sigma}_\odot, \bar{s}_\odot] = [50, 180, 30\,\mathrm{eV}^{-1}]$mbarn with $[\alpha, \beta] = [\frac{1}{3}, 2.7]$. Here we draw a horizontal line for BG by the use of the least square method so that the histogram is well reproduced, where the fitting is applied for $|b| \leq 60°$ as there remain considerable uncertainties in the latitudinal distribution for both the ISM and ISRF *far distant* from the GP, see $\Xi_h(r, z)$ ("h" $\equiv$ H I, H$_2$) in equation (2) and the scale height z_{ph} in equation (7). It is remarkable that the numerical curve is in good agreement with the data not only in shape, but also in absolute value, except the high latitude around the galactic pole.

In Figure 16, we summarize the intensity of BGs obtained by past works, Kappadath et al. (1996) for COMPTEL, Sreekumar et al. (1998) for EGRET, Strong et al. (2004) for EGRET (revised), and Abdo et al. (2010a) for FERMI, where also plotted are those estimated in this work (see Figs. 15 and 17) for the reference, six points (*open circles*) for EGRET and one point (*filled circle*) for FERMI. We draw a broken line given by Abdo et al. with $dI_{\mathrm{BG}}/dE_\gamma = 9.6 \cdot 10^{-3} \times E_\gamma^{-2.41}$ in units of $[\mathrm{cm}^{-2}\mathrm{s}^{-1}\mathrm{sr}^{-1}\mathrm{MeV}^{-1}]$ with E_γ in MeV, and a solid curve with $dI_{\mathrm{BG}}^*/dE_\gamma = dI_{\mathrm{BG}}/dE_\gamma \times [1 - \exp{(-0.33E_\gamma^{0.4})}]$, used in the present work, slightly modifying the FERMI result in the low energy region, while the modification does not affect any change for the results. Significant difference between EGRET and FERMI, with the former giving much harder spectrum than the latter, might be due to a diffrent model in CR propagation as well as those in ISM and ISRF.
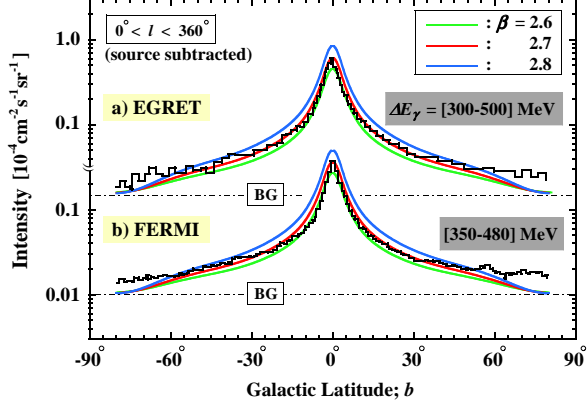
Fig. 17.— Latitudinal distributions of Dγ's obtained by a) EGRET (Hunter et al. 1997) with the energy range 300–500 MeV, and b) FERMI (Porter 2009) with the energy range 350–480 MeV, both averaged over the the whole radial direction, $l = 0°$–$360°$, where drawn are three curves with $\beta = 2.6$ (*green*), 2.7 (*red*), and 2.8 (*blue*), taking the BG contributions into account.

6.3.2. Spatial distribution

We present two examples of the latitudinal distributions for EGRET and FERMI (Porter 2009) with the energy interval around [300–500] MeV in Figures 17a and 17b respectively, together with our numerical results taking the BG contribution (*broken-dotted lines*) into account mentioned above, $dI^*_{\mathrm{BG}}/dE_\gamma$, where plotted are three curves for each figure with $\beta = 2.6$ (*green*), 2.7 (*red*), and 2.8 (*blue*). One finds the agreement between the data and the curves is excellent except the high latitude $|b| \gtrsim 60°$. In these calculations, we take the angular resolution (PSF) effect with the energy dependence into account, for instance, with $7°$ (HWHM) at 30–50 MeV (Hunter et al. 1997).

Corresponding to the latitudinal distributions as shown in Figures 17a and 17b, we demonstrate the longitudinal distributions near the GP in Figures 18a and 18b, where numerical curves are shifted by $\Delta l = +10°$ in both EGRET and FERMI so that experimental data are reproduced more satisfactorily. Again we find the numerical results are in nice agreement with the data in both shape and absolute value, and consistent with $\beta \sim 2.7$.
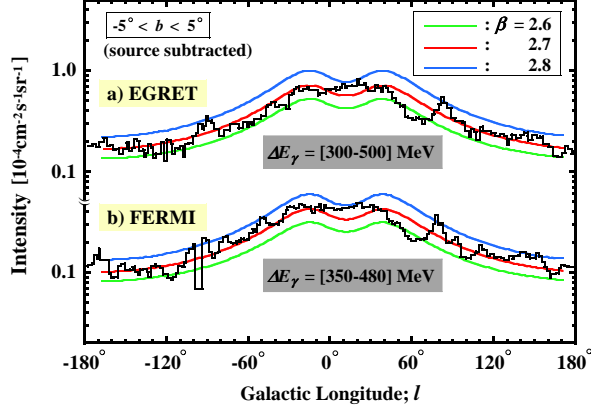
Fig. 18.— Same as Figure 17, but for longitudinal distribution with the same condition, where BG contributions are not presented.
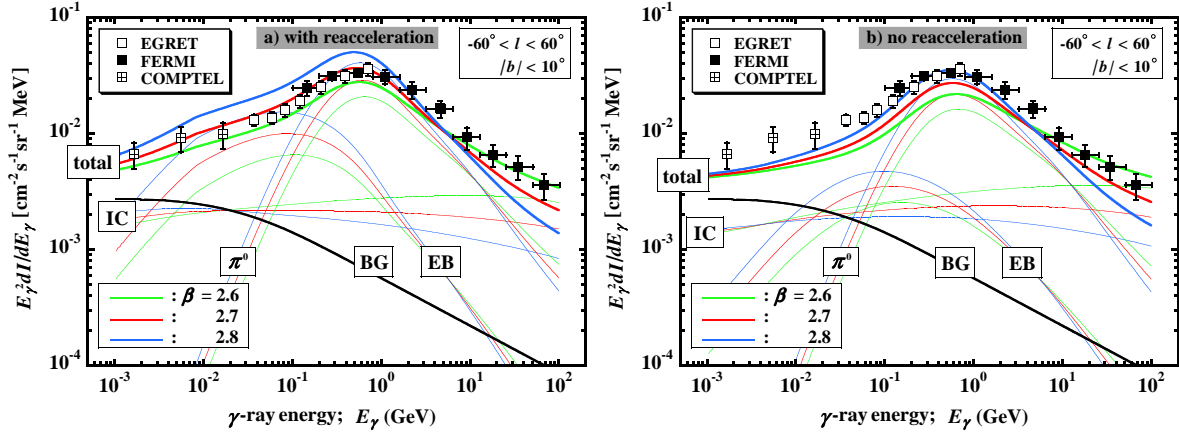

Fig. 19.— Differential energy spectra of Dγ's averaged over the whole radial direction with $|b| < 10°$ obtained by COMPTEL (Kappadath et al. 1996), EGRET (Hunter et al. 1997) and FERMI (Abdo et al. 2010b). Numerical curves are demonstrated for two cases, a) with the reacceleration and b) no reacceleration, each presented separately for individual components.

6.3.3. Energy spectrum

First, in Figure 19a we present the energy spectrum of Dγ's averaged over the field of view with $-60° < l < 60°$ and $|b| < 10°$, where numerical curves with the reacceleration are also presented separately for those coming from π^0, EB, and IC (all with *colored thin solid curves*), BG (*heavy black solid curve*), and total (*colored heavy solid curves*). Here and in
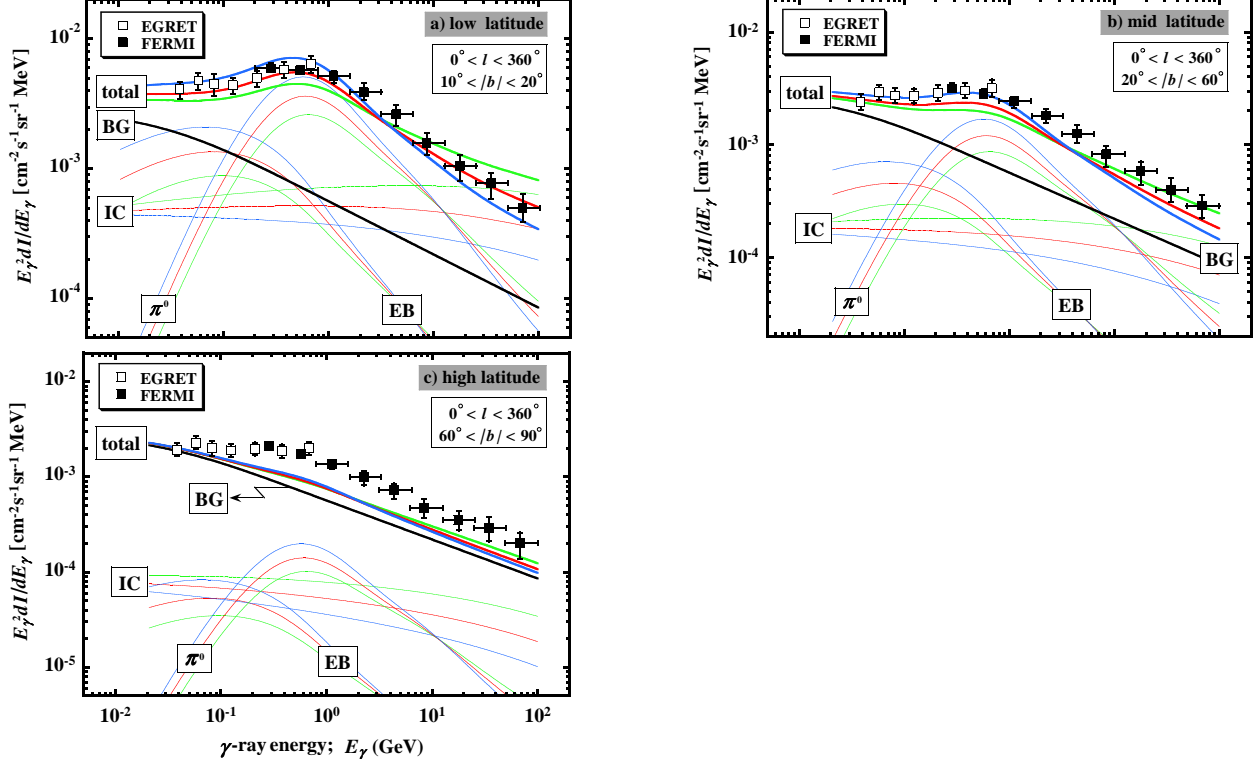
Fig. 20.— Same as Figure 19a, but those averaged over three different ranges in the galactic latitude, a) low latitude with $10° < |b| < 20°$, b) mid latitude with $20° < |b| < 60°$, and c) high latitude with $60° < |b| < 90°$. Parameter sets for the numerical calculations are the same as those used in Figure 19a with the reacceleration.

the following we omit EGRET data in GeV region, because of the instrumental problem in detection of γ's (Stecker et al. 2008). One finds that the curve with $\beta = 2.7$ (red) is in good agreement with the data in the energy region below 1 GeV, while they deviate slightly from the curve above 1 GeV, with approximately 20% enhancement.

Figure 19b reproduces Figure 19a, but for curves without reacceleration, corresponding to Figures 11b and 13b (see also Fig. 8b). The fit is not as good as for the reacceleration model, particularly in the low energy region, $E_\gamma \lesssim 200$ MeV, with $\sim 40\%$ enhancement, while with $\sim 20\%$ in the high energy region, $E_\gamma \gtrsim 1$ GeV, giving nearly the same enhancement as in the case of (a) with the reacceleration.

Second, in Figures 20 and 21, we present the energy spectra of Dγ's for different sky views (Abdo et al. 2010a; see also supplementary material at http://link.aps.org/supplement-al/10.1103/Ph Figure 20 shows those averaged over independent galactic latitude ranges covering low, mid and high galactic latitudes, a) $10° < |b| < 20°$, b) $20° < |b| < 60°$ and c) $60° < |b| < 90°$ respec-
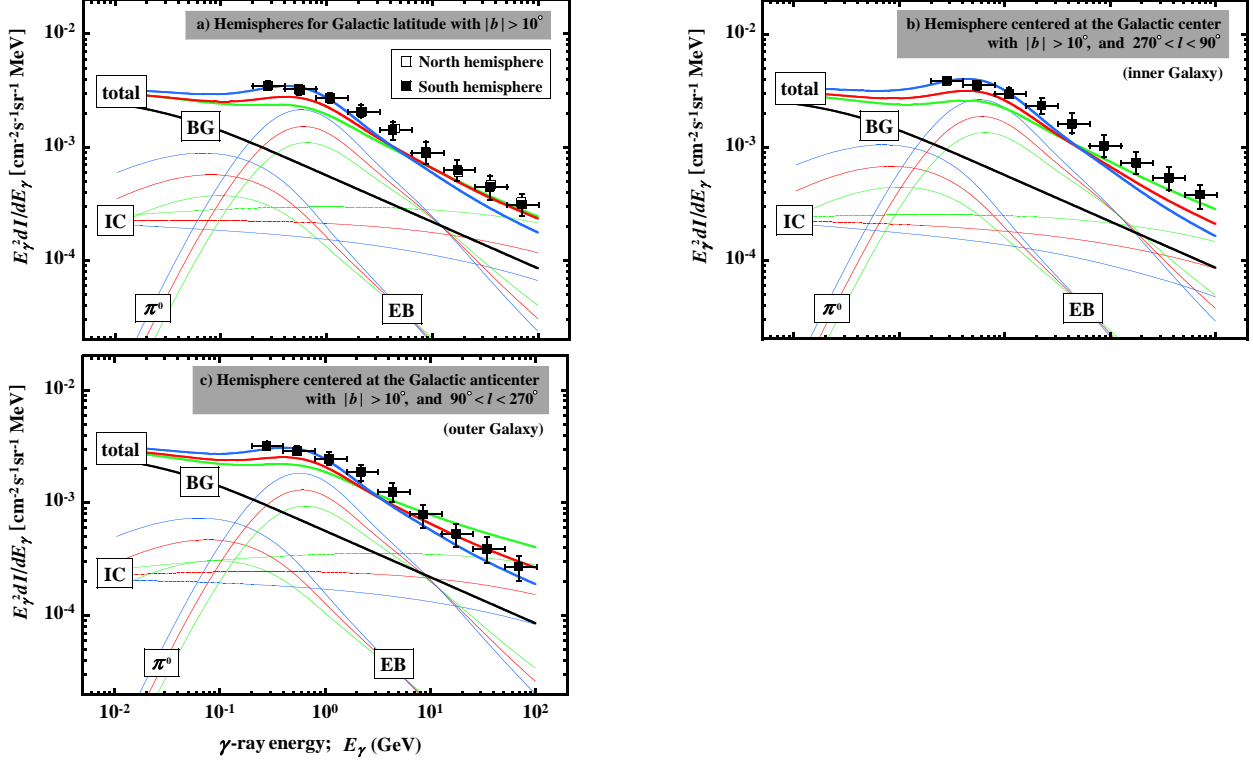
Fig. 21.— Same as Figure 20, but those averaged over different hemispheres on the sky for the galactic latitudes with $|b| > 10°$, which are centered at a) the north galactic pole (*open square*) and the south galactic pole (*filled square*), b) the galactic center with $270° < l < 90°$ (inner Galaxy), and c) the anticenter $90° < l < 270°$ (outer Galaxy).

tively. Figure 21 shows those averaged over different hemishperes, which are, a) centered at the north ($b \geq 0°$; *open squares*) and south ($b \leq 0°$; *filled squares*) galactic poles, b) the galactic center ($270° \leq l \leq 90°$), and c) anticenter ($90° \leq l \leq 270°$), all with the galactic latitudes excluding $|b| < 10°$. In these figures, we subtract γ's coming from point sources based on the FERMI catalog.

It is remarkable in Figure 20 that EGRET and FERMI data agree pretty well with each other, overlapping nicely around 0.2–1GeV, in all latitude ranges. One finds that the numerical curves with $\beta = 2.7$ reproduce generally well both the EGRET and FERMI data in Figures 20 and 21 but 20c, taking account of the uncertainties in various galactic parameters, particularly in those related to the ISM and ISRF.

On the other hand, in Figure 20c for the high latitude, $|b| > 60°$, we have a noticeable enhancement in FERMI with approximately 70% as compared to the numeical curves. To see the deviation more clearly, we present them all together in Figure 22, where we show ad-
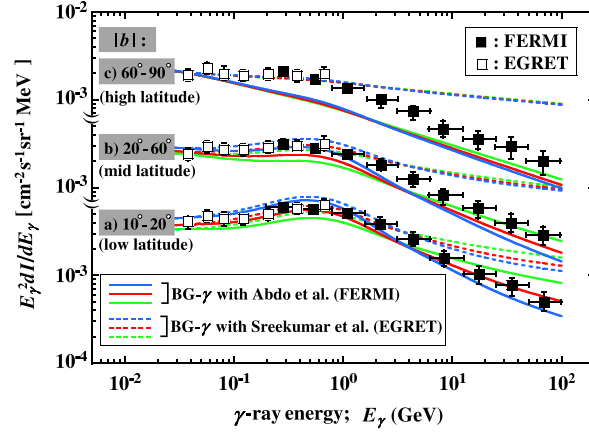
Fig. 22.— Same as Figure 20, but two cases of numerical curves, a) with the BG-γ given by FERMI (Abdo et al. 2010a) (*solid curves*), and b) with the BG-γ by EGRET (Sreekumar et al. 1998) (*dotted curves*).
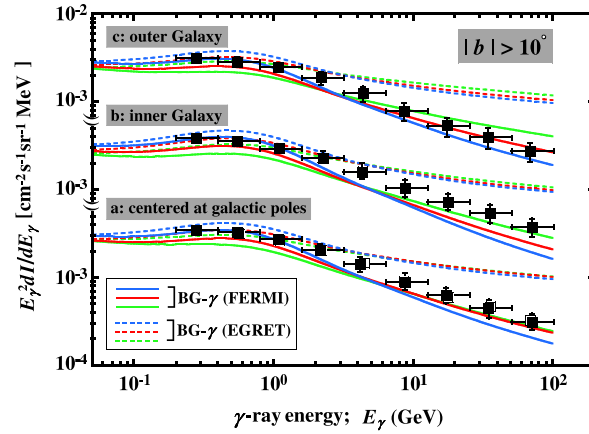

Fig. 23.— Same as Figure 21, but two cases of numerical curves, a) with the BG-γ given by FERMI (Abdo et al. 2010a) (*solid curves*), and b) with the BG-γ by EGRET (Sreekumar et al. 1998) (*dotted curves*).

ditionally numerical curves (*dotted colors*) using EGRET-BG obtained by Sreekumar (1998) for reference (see Fig. 16). Figure 23 reproduces Figure 21 with numerical curves using EGRET-BG (*dotted colors*) in addition to those using FERMI-BG (*solid colors*).

One finds the spectrum shapes with EGRET-BG are quite different from the data in the high energy region, although the enhancement is rather improved in the energy region $\lesssim 1\,\mathrm{GeV}$, which is discussed again in the next section.

7.   Discussion and summary

We have studied the diffusion-halo model with stochastic reacceleration, comparing it with the most recent data on hadronic, electronic and Dγ components. We have two particular interests: to find an unified model for the CR acceleration and propagation from the viewpoint of astrophysics, and to search for a signal of novel sources such as PBH and/or DM from the viewpoints of particle physics and cosmology. Both are of course closely connected with each other in the sense that the knowledge of the former is decisive in confirming the latter. While several groups (Torii et al. 2006; Chang et al. 2008) have reported the possibility of annihilation and/or decay of DM particles, giving a significant bump in electron flux around $500\,\mathrm{GeV}$, FERMI (Abdo et al. 2009) and H.E.S.S. (Aharonian et al. 2009) give a rather flat spectrum up to $1\,\mathrm{TeV}$ without the prominent excess. In the present paper, however, we have focussed our interest rather conservatively on the internal consistency among various CR components from the view point of astrophysics, leaving the puzzle of the possible electron/positron-excess to further observations and mutual cross-checks in data analysis among individual groups.

In our past works on the hadronic component, we concluded that the diffusion-halo model with the reacceleration with the parameter set, $[\zeta_0, \bar{\sigma}_\odot] = [50, 180]$ mbarn with $[\alpha, \beta] = [\frac{1}{3}, 2.7$–$2.8]$, is in harmony with the CR hadron data presently available. The most recent data on the B/C ratio by CREAM and TRACER (Fig. 11) as well as on the $\bar{p}/p$ ratio by PAMELA (Fig. 12) also support the present model. However, it is worth mentioning here that our interpretation for the energy dependence of the B/C ratio is somewhat different from that by CREAM (Ahn et al. 2008) and TRACER (Müller 2009).

They claim that the index α favors 0.5–0.6 instead of $\frac{1}{3}$, resulting in a rapid decrease with energy for the interstellar propagation path length. In contrast to their interpretation, we would like to point out that the value of 0.5–0.6 is not *fundamental*, but is rather *accidental* due to the reacceleration effect, namely it is boosted upward around the GeV region by the energy gain, resulting coincidentally in the soft slope with 0.5–0.6 in the energy region 1–100 GeV. The intrinsic one must be $\frac{1}{3}$ (Kolmogorov-type for wave number spectrum in hydromagnetic turbulence), leading to 1) a natural drop in path length distribution in the low energy region $\lesssim 1\,\mathrm{GeV}$ without introducing an artificial break there, as originally proposed by Simon et al. (1986), and 2) a reasonable amplitude in the anisotropy of CR's with the level of 10^{-3} in TeV region nowadays established experimentally.

We apply the diffusion-halo model with and without the stochastic reacceleration for the electron and Dγ components. Apart from the electron-anomaly around $500\,\mathrm{GeV}$, we find that the parameter set with the reacceleration, $[\alpha, \beta; \zeta_0, \bar{\sigma}_\odot]$, expected from hadron component reproduces rather well both the spectrum shape and the absolute value in both the electron

(Fig. 13a) and Dγ (Figs. 17–21) components, assuming the additional parameter $\bar{s}_\odot$ with 20–30 eV^{-1}mbarn. Physical meanings of the numerical set with $[\zeta_0, \bar{\sigma}_\odot] = [50, 180]$ mbarn are discussed in Papers I–III in connection with the diffusion constant $D_\odot$, gas density $\bar{n}_\odot$, their scale heights, z_D, z_n, etc, giving reasonable values matched with the observtional data.

Let us consider the physical meaning of 20–30 eV^{-1}mbarn in $\bar{s}_\odot$. The relation between $\bar{\sigma}_\odot$ and $\bar{s}_\odot$ is given by

$$\frac{\bar{s}_\odot}{\bar{\sigma}_\odot} = \frac{\bar{n}_\odot}{\bar{\epsilon}_\odot} \frac{1 + 1/\kappa}{1 + 1/\nu} = \frac{\bar{n}_\odot}{\bar{\epsilon}_\odot} \frac{2 + z_D/z_\epsilon}{2 + z_D/z_n},$$

see § 4.2 for $\bar{s}_\odot$ and $\bar{\sigma}_\odot$ with $r = r_\odot$, and Table 4 for ν and κ. Namely, it is closely related to the ratio of the energy density $\bar{\epsilon}_\odot$ to the gas density $\bar{n}_\odot$ at the SS, for the *smeared* energy density, *smeared* gas density respectively, and three latitudinal scale heights, z_ϵ, z_n and z_D. As discussed in §§ 2 and 3.1, we have $n_\odot = n_{\mathrm{HI}}^\odot + n_{\mathrm{H}_2}^\odot + n_{\mathrm{HII}}^\odot = 1.14 \mathrm{H}$ atoms cm^{-3}, and $\epsilon_\odot = \epsilon_{\mathrm{B}}^\odot + \epsilon_{\mathrm{ph}}^\odot \approx 2.3$ eV cm^{-3}, leading to $\epsilon_\odot/n_\odot \approx 2$ eV. Remembering that the scale heights used in the present paper are $[z_n, z_\epsilon; z_D] = [0.2, 0.75; 3.0]$ kpc, we find $\bar{s}_\odot = 32$ eV^{-1}mbarn for $\bar{\sigma}_\odot = 180$ mbarn, giving a consistent result, while the latter with 180 mbarn is expected from the relation, $\bar{\sigma}_\odot \simeq D_\odot/[\bar{n}_\odot c z_D z_n]$ with a reasonable set $[D_\odot, \bar{n}_\odot] = [3 \times 10^{28}\,\mathrm{cm}^2\,\mathrm{s}^{-1},\ 1\,\mathrm{cm}^{-3}]$ and $[z_D, z_n] = [3, 0.2]$ kpc as discussed in Papers I, II.

As mentioned above, the electron spectra currently available are *generally* in agreement with those expected from the hadron spectra, considering the uncertainties inherent in both the experimental data and the numerical parameters, but not quite satisfactory, with the FERMI data giving the excess by 20–30% around several hundred GeV compared to the numerical results as seen in Figure 14. It might be related to the positron excess around 10–100 GeV observed by PAMELA (Adriani et al. 2009), indicating some nearby sources and/or exotic ones from DM annihilation or decay, while beyond the subject of the present paper. In fact most recently Delahaye et al. (2010) show that the electron spectra with FERMI, HESS and PAMELA are reproduced rather well by the standard astrophysical processes, assuming two sources separately, the distant and local nearby ones, whereas they stress that there remain too large theoretical uncertainties to build a standard model for CR electrons. So it is critical to study the Dγ's and diffuse radio emissions simultaneously in order to reduce the uncertainties inherent in the galactic parameters assumed for the numerical calculations.

We compared our numerical results on the energy spectrum of Dγ's with EGRET and FERMI data for several sets of the field of view (Figs. 17–21), and found that overall, the CR data, hadron (Fig. 6 in Paper V) and electron (Fig. 14) components, reproduce rather satisfactorily Dγ's for both EGRET and FERMI, considering the fact that we have uncertainties with at least 10–20% in the galactic parameters assumed here as well as in the flux normalization of the hadron and electron components. Small enhancements of Dγ's in

GeV region (Figs. 19, 20), albeit they are still within the uncertainties, may indicate those from nearby sources such as the supernova remnants, pulsars, and pusar wind nebulae.

We found, however, that FERMI data give the significant excess with approximately 70% or more in the *high latitude* (Fig. 22), well beyond the uncertaities, against the numerical results in GeV region. This result may indicate a signature of very large electron-halo far distant from the GP, with, for instance, as large as 25kpc (Keshet et al. 2004), and/or something else coming from the cosmological origin. We are also concerned if the exess here discussed relates to those appearing in the electron spectrum between 100 and 1000GeV observed by FERMI and HESS (Fig. 14) and in the positron spectrum around several tens GeV by PAMELA. To make clear the correlation between these excesses, Dγ's in the high latitude and the electrons/positrons around several tens to hundred GeV, crucially important is the anisotropy study for the high energy electron, which will be discussed elsewhere in the near future.

Finally we briefly argue the electron spectrum obtained by FERMI from the observational point of view, aside from the prominent bumps indicated by ATIC and PPB-BETS. FERMI is indeed excellent in the observation for γ-rays, we have some concerns about the separation of electrons from hadrons as well as their energy determination in the high energy region, while acknowledging the team have studied very carefully the reliability from various kinds of checks, with both beam tests and the simulational analyses.

Nevertheless, one should keep in mind that FERMI is not *purely-direct* observations for electrons, but *quasi-direct* ones in the sense that electron events are selected by *statistical* analysis based on simulations for the spread of electron showers, where a small number of electrons are statistically selected from a large proton background. In contrast to these quasi-direct experiments, the PAMELA apparatus consists of a permanent magnetic spectrometer with a silicon tracking system, providing good identification between electrons and positrons, though limited to a maximum detectable rigidity (MDR) of 100 GV.

Anyway, we await further studies and mutual cross-checks among the groups from various points of view to get a firm conclusion for the electron-excess around 500GeV, while not so prominent as given by ATIC and PPB-BETS. So results from the AMS program (Bindi 2009), AMS-02, will be of particular interest. This program aims at high precision measurements of CR (both electron and hadron) and γ-ray fluxes from a few hundred MeV to a few TeV using a super-conducting magnet[1], with the space shuttle launch scheduled for September 2010. We also look forward to Dγ's data from ground-based telescopes currently

---

[1]After submitting the present paper, we find that they decided to use the permanent magnet in place of the super-conducting magnet (Kounine 2010).

operating such as H.E.S.S., MAGIC, and VERITAS, as well as the CTA-program now under consideration (Caballero et al. 2008), the threshold energies of which are now overlapping with the FERMI satellite data.

APPENDIX A
ENERGY LOSS OF ELECTRONS IN ISM and ISRF

The energy-loss rate due to the bremsstrahlung in the gas density $n(\boldsymbol{r})$ is given by

$$-\Big\langle \frac{\Delta E_e}{\Delta t}\Big\rangle_{\text{rad}} = \int_0^{E_e} E_\gamma [n(\boldsymbol{r})c\sigma_{\text{EB}}(E_e, E_\gamma)]dE_\gamma = n(\boldsymbol{r})w_{\text{rad}}(E_e)E_e, \qquad (A1)$$

where

$$w_{\text{rad}}(E_e) = w_{\text{EB}}^{(0)} \int_0^1 \phi_{\text{EB}}(x, E_e x)dx,$$

with

$$w_{\text{EB}}^{(0)} = c\sigma_{\text{EB}}^{(0)} = 4c\alpha_f Z(Z+1)\Big(\frac{e^2}{m_e c^2}\Big)^2 = 1.39 \times 10^{-16} \text{cm}^3\text{s}^{-1},$$

for hydrogen atoms, and see the left-hand side of Table 5 for $\phi_{\text{EB}}(x, E_\gamma)$.

For $E_e \gg m_e c^2$, we can use the complete screening cross-section, leading to the well-known result

$$-\Big\langle \frac{\Delta E_e}{\Delta t}\Big\rangle_{\text{rad}} = n(\boldsymbol{r})w_{\text{rad}}^{(\infty)}E_e; \quad w_{\text{rad}}^{(\infty)} = 7.30 \times 10^{-16} \text{cm}^3\text{s}^{-1}.$$

On the other hand the energy-loss rate due to the IC is given, taking into account the energy spectrum of the target photon at $\boldsymbol{r}$, $n_{\text{ph}}(\boldsymbol{r}; E_{\text{ph}})$, by

$$-\Big\langle \frac{\Delta E_e}{\Delta t}\Big\rangle_{\text{IC}} = \int_0^\infty dE_{\text{ph}} \int_{E_{\text{ph}}}^{E_{\text{M}}} E_\gamma [n_{\text{ph}}(\boldsymbol{r}; E_{\text{ph}})c\sigma_{\text{IC}}(E_e, E_\gamma; E_{\text{ph}})]dE_\gamma, \qquad (A2)$$

with

$$E_{\text{M}} \equiv E_{\text{M}}(E_e, E_{\text{ph}}) = E_e \frac{X}{1+X}; \quad X \equiv X(E_e, E_{\text{ph}}) = \frac{4E_{\text{ph}}E_e}{(m_e c^2)^2}, \qquad (A3)$$

see the right-hand side of Table 5 for $\sigma_{\text{IC}}(E_e, E_\gamma; E_{\text{ph}})$. Here we omit the suffix i introduced in §2.2 for simplicity. For $E_e \gg m_e c^2$, equivalently $X \gg 1$, one finds a reasonable result, $E_{\text{M}} \approx E_e$, leading to $E_{\text{ph}} \le E_\gamma \le E_e$.

From equation (4) in the text

$$n_{\mathrm{ph}}(\boldsymbol{r}; E_{\mathrm{ph}})dE_{\mathrm{ph}} = \left[\frac{\epsilon_{\mathrm{ph}}(\boldsymbol{r})}{k_{\mathrm{B}}T_{\mathrm{ph}}}\right]W_{\mathrm{ph}}(k)\frac{dk}{k^2}; \quad k = \frac{E_{\mathrm{ph}}}{k_{\mathrm{B}}T_{\mathrm{ph}}},$$

where $W_{\mathrm{ph}}(k)$ is the Planck function for the 2.7 K CMB, and the gaussian function given by equation (5) for the stellar radiation and the re-emission from the dust grains.

The integration with respect to E_γ is given (Jones 1965, 1968) by, (see eq. [A3] for X)

$$\int_{E_{\mathrm{ph}}}^{E_{\mathrm{M}}} E_\gamma \sigma_{\mathrm{IC}}(E_e, E_\gamma; E_{\mathrm{ph}})dE_\gamma \approx \sigma_{\mathrm{IC}}^{(0)} E_e S_{\mathrm{IC}}(X)/X^2,$$

with

$$\sigma_{\mathrm{IC}}^{(0)} = 3\sigma_{\mathrm{T}} = 2.00 \times 10^{-24}\mathrm{cm}^2, \quad (\sigma_{\mathrm{T}}: \text{ Thomson cross-section}),$$

and

$$S_{\mathrm{IC}}(X) = \left(\frac{X}{2} + 6 + \frac{6}{X}\right)\ln(1+X) - \frac{11X^3/12 + 6X^2 + 9X + 4}{(1+X)^2} - 2 - 2\int_0^X \frac{\ln(1+t)}{t}dt.$$

One should note that the approximation used above is only $E_e \gg m_e c^2$, readily satisfying the condition in the energy region of interest, $E_e \gtrsim 10\,\mathrm{MeV}$.

Now, we have the energy-loss rate due to the IC scattering in a compact form after integrating over the energy E_{ph} of the target photon in equation (A2),

$$-\left\langle\frac{\Delta E_e}{\Delta t}\right\rangle_{\mathrm{IC}} = \epsilon_{\mathrm{ph}}(\boldsymbol{r})w_{\mathrm{T}}\Lambda(E_e, T_{\mathrm{ph}})E_e^2, \tag{A4}$$

where E_e is in units of GeV and ϵ_{ph} in eVcm^{-3}, and

$$w_{\mathrm{T}} = \frac{4}{3}\frac{c\sigma_{\mathrm{T}} \times 10^{-9}}{[m_e c^2/\mathrm{GeV}]^2} = 1.018 \times 10^{-16}\mathrm{cm}^3\mathrm{s}^{-1}, \tag{A5}$$

$$\Lambda(E_e, T_{\mathrm{ph}}) \equiv \Lambda(\Theta_e) = 9\int_0^\infty S_{\mathrm{IC}}(X)W_{\mathrm{ph}}(\Theta_e^2 X)dX/X^4, \tag{A6}$$

with

$$\Theta_e \equiv \Theta_e(E_e, T_{\mathrm{ph}}) = \frac{m_e c^2/2}{\sqrt{(k_{\mathrm{B}}T_{\mathrm{ph}})E_e}}. \tag{A7}$$

The above discussions are applicable also for the synchrotron radiation, since it is caused by the collision between an electron and the virtual photon induced by the magnetic field. Practically, however, we have the condition $\hbar\omega_c\Gamma_e \ll m_e c^2$ (Γ_e: Lorentz factor of electron) with $\omega_c = eH_\perp/m_e c^2$, and we can use the Thomson scattering cross-section, namely $\Lambda(E_e, T_{\mathrm{ph}}) \to 1$. Hence we obtain equation (12a).

APPENDIX B
CONTRIBUTION OF PERTURBATIVE TERMS IN THE TRANSPORT EQUATION

B1. HIGH ENERGY REGION $E_e \gtrsim E_c^+$

Since we can neglect the fluctuation due to the reacceleration in the HE region, we take here the second term in equation (25a) alone, omitting the second term in equation (22). The transport equation for the electron density in the HE region, $N_{e,\epsilon}^{(0)}(\boldsymbol{r}; E_e, t)$, without the perturbative term, is given by

$$\left[\frac{\partial}{\partial t} - \nabla \cdot D(\boldsymbol{r}; E_e)\nabla - \bar{\epsilon}(\boldsymbol{r})\frac{\partial}{\partial E_e}\mathcal{W}_\epsilon(E_e)\right] \cdot N_{e,\epsilon}^{(0)}(\boldsymbol{r}; E_e, t) = Q(\boldsymbol{r}; E_e, t).$$

As discussed in § 4.1, we regard $N_{e,\epsilon}^{(0)}(\boldsymbol{r}; E_e, t)$ as the solution of the first order approximation for equation (21), so that we have the following equation with the perturbative term, $\bar{n}(\boldsymbol{r})[\mathcal{W}_n(E_e)N_{e,\epsilon}^{(0)}(\boldsymbol{r}; E_e, t)]'$, moving it to the right-hand side,

$$\left[\frac{\partial}{\partial t} - \nabla \cdot D(\boldsymbol{r}; E_e)\nabla - \bar{\epsilon}(\boldsymbol{r})\frac{\partial}{\partial E_e}\mathcal{W}_\epsilon(E_e)\right] \cdot N_{e,\epsilon}(\boldsymbol{r}; E_e, t) = Q(\boldsymbol{r}; E_e, t) + \bar{n}(\boldsymbol{r})\frac{\partial}{\partial E_e}\mathcal{W}_n(E_e)N_{e,\epsilon}^{(0)}(\boldsymbol{r}; E_e, t).$$

Now, we rewrite the solution

$$N_{e,\epsilon}(\boldsymbol{r}; E_e, t) = N_{e,\epsilon}^{(0)}(\boldsymbol{r}; E_e, t) + \tilde{N}_{e,n}^{(0)}(\boldsymbol{r}; E_e, t),$$

leading to

$$\left[\frac{\partial}{\partial t} - \nabla \cdot D(\boldsymbol{r}; E_e)\nabla - \bar{\epsilon}(\boldsymbol{r})\frac{\partial}{\partial E_e}\mathcal{W}_\epsilon(E_e)\right] \cdot \tilde{N}_{e,n}^{(0)}(\boldsymbol{r}; E_e, t) = \bar{n}(\boldsymbol{r})\frac{\partial}{\partial E_e}\mathcal{W}_n(E_e)N_{e,\epsilon}^{(0)}(\boldsymbol{r}; E_e, t).$$

Thus for the steady state ($\partial/\partial t = 0$), we have the solution of the second order approximation

$$\tilde{N}_{e,n}^{(0)}(\boldsymbol{r}; E_e) = \int_0^\infty \tilde{\Pi}_\epsilon^{(0)}(\boldsymbol{r}; y)\tilde{f}_n^{(0)}(y; E_e)dy,$$

with

$$\left[\bar{\epsilon}(\boldsymbol{r})c\frac{\partial}{\partial y} - \nabla \cdot D(\boldsymbol{r})\nabla\right] \cdot \tilde{\Pi}_\epsilon^{(0)}(\boldsymbol{r}; y) = \tilde{Q}^{(0)}(\boldsymbol{r})\delta(y),$$

$$\left[cE_e^\alpha\frac{\partial}{\partial y} - \frac{\partial}{\partial E_e}\mathcal{W}_\epsilon(E_e)\right] \cdot \tilde{f}_n^{(0)}(y; E_e) = 0,$$

where $\tilde{Q}^{(0)}(\boldsymbol{r})$ and $\tilde{f}_n^{(0)}(0; E_e)$ are given by replacing $Q^{(0)}(\boldsymbol{r})$ [$\equiv Q(\boldsymbol{r})$] and $f_\epsilon^{(0)}(0; E_e)$ (see eqs. [24b] and [28b]) with

$$Q^{(0)}(\boldsymbol{r}) = Q_0 e^{-r/r_Q - |z|/z_Q} \Rightarrow \tilde{Q}^{(0)}(\boldsymbol{r}) = \bar{n}(\boldsymbol{r})e^{-|z|/z_D}\frac{2Q_0}{\bar{\epsilon}_0}\frac{\mathcal{J}_\kappa(\omega_\kappa, U_\kappa)}{J_\kappa(U_\kappa)},$$

$$f_\epsilon^{(0)}(0; E_e) = E_e^{-\gamma-\alpha} \;\; \Rightarrow \;\; \tilde{f}_n^{(0)}(0; E_e) = E_e^{-\alpha}\frac{1}{c}\frac{\partial}{\partial E_e}\Big[\mathcal{W}_n(E_e)F_{r,\epsilon}^{(0)}(E_e)\Big],$$

with

$$\mathcal{J}_\kappa(\omega, U) = \int_0^1 t^\omega J_\kappa(Ut)dt,$$

see Table 4 for κ, ω_κ, and U_κ, and $J_\kappa(U)$ is the Bessel function of the index with κ (Paper I).

Corresponding to the replacement of $Q^{(0)}(\boldsymbol{r}) \Rightarrow \tilde{Q}^{(0)}(\boldsymbol{r})$, the scale heights in the source, r_Q and z_Q, must be replaced as

$$\frac{1}{r_Q} \;\Rightarrow\; \frac{1}{r_n}, \quad \frac{1}{z_Q} \;\Rightarrow\; \frac{1}{z_n} + \frac{1}{z_D} = \frac{2}{\bar{z}_n},$$

leading to the following replacements,

$$\omega_\kappa = \Big(\frac{1}{z_Q} - \frac{1}{2z_\epsilon}\Big) \;\Rightarrow\; \Big(\frac{2}{\bar{z}_n} - \frac{1}{2z_\epsilon}\Big) \equiv \tilde{\omega}_\kappa,$$

while the radial scale height in the source, r_Q, doesn't appear explicitly in this procedure.

Now the Laplace transform of $\tilde{f}_n^{(0)}(y; E_e)$ is immediately given (see eq. [31]) by

$$\frac{\tilde{F}_{r,n}^{(0)}(E_e)}{F_{r,\epsilon}^{(0)}(E_e)} = \int_{E_e}^\infty dE_0 \frac{[\mathcal{W}_n(E_0)F_{r,\epsilon}^{(0)}(E_0)]'}{\mathcal{W}_\epsilon(E_e)F_{r,\epsilon}^{(0)}(E_e)}\,\mathrm{e}^{-Y_{r,\epsilon}(E_e, E_0)}, \tag{B1}$$

where $[\cdots]'$ denotes the differential with respect to E_0, and see §4.2 for $Y_{r,\epsilon}(E_e, E_0)$, and we obtain

$$\frac{\tilde{N}_{e,n}^{(0)}(\boldsymbol{r}; E_e)}{N_{e,\epsilon}^{(0)}(\boldsymbol{r}; E_e)} = \frac{2}{\bar{\eta}_0}\frac{\mathcal{J}_\kappa(\tilde{\omega}_\kappa, U_\kappa)}{J_\kappa(U_\kappa)}\frac{\tilde{F}_{r,n}^{(0)}(E_e)}{F_{r,\epsilon}^{(0)}(E_e)}, \tag{B2}$$

with

$$\bar{\eta}_r = \bar{\epsilon}_r/\bar{n}_r = \bar{\eta}_0\mathrm{e}^{-2r(1/\bar{r}_\epsilon - 1/\bar{r}_n)}; \quad \bar{\eta}_0 = \bar{\epsilon}_0/\bar{n}_0.$$

In Figure 24a, we show $\tilde{N}_{e,n}^{(0)}(\boldsymbol{r}; E_e)/N_{e,\epsilon}^{(0)}(\boldsymbol{r}; E_e)$ against E_e at the SS with $[\bar{\eta}_\odot, \bar{r}_\epsilon] = [2\,\mathrm{eV}, 8\,\mathrm{kpc}]$, corresponding to $[\bar{\epsilon}_\odot, \bar{n}_\odot] = [2\,\mathrm{eVcm}^{-3}, 1\,\mathrm{cm}^{-3}]$. Then one finds that the perturbative contribution due to the energy change in proportion to the gas density, $\bar{n}(\boldsymbol{r})$, is less than 10% in the energy region $E_e \gtrsim E_c^+$.

We finally obtain

$$N_{e,\epsilon}(\boldsymbol{r}; E_e) = \frac{2Q_0}{\bar{\epsilon}_0}\frac{\mathcal{J}_\kappa(\omega_\kappa, U_\kappa)}{J_\kappa(U_\kappa)}F_{r,\epsilon}(E_e)\mathrm{e}^{-|z|/z_D}, \tag{B3}$$

with

$$F_{r,\epsilon}(E_e) = F_{r,\epsilon}^{(0)}(E_e) + \frac{2}{\bar{\eta}_0}\frac{\mathcal{J}_\kappa(\tilde{\omega}_\kappa, U_\kappa)}{J_\kappa(U_\kappa)}\tilde{F}_{r,n}^{(0)}(E_e). \tag{B4}$$

B2. LOW ENERGY REGION $E_e \lesssim E_c^+$

In the LE region, the fluctuation term due to the reacceleration , $\langle \Delta E_e^2 / \Delta t \rangle_{\mathrm{rea}}$, becomes now effective as compared to the *average* energy-loss term due to the synchrotron-IC effect, $\langle \Delta E_e / \Delta t \rangle_{\mathrm{sic}}$, in proportion to the energy density, $\bar{\epsilon}(\boldsymbol{r})$. So equation (25b) is approximately written as

$$\bar{n}(\boldsymbol{r})\mathcal{W}_n(E_e) + O[\bar{\epsilon}(\boldsymbol{r})\mathcal{W}_\epsilon(E_e)] \simeq \bar{n}(\boldsymbol{r})[\mathcal{W}_n(E_e) + \bar{\eta}_* \mathcal{W}_\epsilon(E_e)], \tag{B5}$$

with

$$\bar{\epsilon}(\boldsymbol{r})/\bar{n}(\boldsymbol{r}) \approx \left\langle \bar{\epsilon}(\boldsymbol{r})/\bar{n}(\boldsymbol{r}) \right\rangle_{\mathrm{eff}} \equiv \bar{\eta}_*, \tag{B6}$$

where the *effective* value of $\bar{\eta}_*$ is of the magnitude of $[1\text{–}5]\,\mathrm{eV}$, and for instance $\bar{\eta}_* = \bar{\eta}_\odot \approx 2\,\mathrm{eV}$ at the SS.

Neglecting the second term in equation (B5), we have the solution for the principal term, corresponding to equation (32), (see §3.3 and Table 4 for ν, U_ν)

$$N_{e,n}^{(0)}(\boldsymbol{r}; E_e) = \frac{2Q_0}{\bar{n}_0 c} \frac{\mathcal{J}_\nu(\omega_\nu, U_\nu)}{J_\nu(U_\nu)} F_{r,n}^{(0)}(E_e)\mathrm{e}^{-|z|/z_D}, \tag{B7}$$

with

$$F_{r,n}^{(0)}(E_e) = \frac{c}{|\mathcal{W}_n(E_e)|} \int_{E_{\min}}^{E_{\max}} dE_0 E_0^{-\gamma} \mathrm{e}^{-Y_{r,n}(E_e, E_0)}, \tag{B8}$$

and

$$Y_{r,n}(E_e, E_0) = c\bar{\sigma}_r \int_{E_e}^{E_0} \frac{E^\alpha}{\mathcal{W}_n(E)} dE. \tag{B9}$$
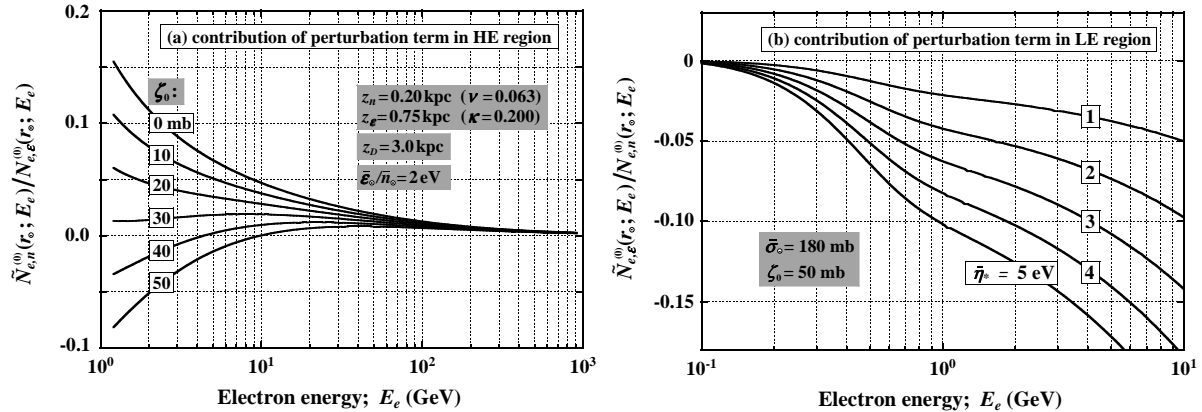

Fig. 24.— Numerical results of the contribution of the perturbative terms in the (a) HE region and (b) LE region.

Now putting

$$\mathcal{W}_n^*(E_e) = \mathcal{W}_n(E_e) + \bar{\eta}_* \mathcal{W}_\epsilon(E_e),$$

the electron density with the synctrotron-IC effect (perturbative term here) is immediately

$$N_{e,n}^{*(0)}(\boldsymbol{r}; E_e) = \frac{2Q_0}{\bar{n}_0 c} \frac{\mathcal{J}_\nu(\omega_\nu, U_\nu)}{J_\nu(U_\nu)} F_{r,n}^{*(0)}(E_e) e^{-|z|/z_D}, \tag{B10}$$

where $F_{r,n}^{*(0)}(E_e)$ is given by replacing $\mathcal{W}_n$ with $\mathcal{W}_n^*$ in equations (B8) and (B9), and it is related to the perturbvative term, $\tilde{N}_{e,\epsilon}^{(0)}$, discussed in §4.1 as

$$N_{e,n}^{*(0)}(\boldsymbol{r}; E_e) = N_{e,n}^{(0)}(\boldsymbol{r}; E_e) + \tilde{N}_{e,\epsilon}^{(0)}(\boldsymbol{r}; E_e). \tag{B11}$$

Here one should be careful of the integral range of E_0 in equation (B8), $[E_{\min}, E_{\max}]$, since we have two zero points in $\mathcal{W}_n^*(E_e)$ at two energies, E_{c*}^- and E_{c*}^+, for instance, $[E_{c*}^-, E_{c*}^+] \approx [0.1, 1]\,\mathrm{GeV}$ for $\zeta_0 = 50\,\mathrm{mbarn}$ and $\bar{\eta}_* = 2\,\mathrm{eV}$, and

$$[E_{\min}, E_{\max}] = \begin{cases} [E_e, \ E_{c*}^-] & \text{for} & E_e < E_{c*}^-, \\ [E_{c*}^-, \ E_e] & \text{for} & E_{c*}^- < E_e < E_{c*}^+, \\ [E_e, \ +\infty] & \text{for} & E_e > E_{c*}^+. \end{cases}$$

We present $\tilde{N}_{e,\epsilon}^{(0)}/N_{e,n}^{(0)}$ against E_e for several sets of $[\bar{\eta}_*; z_n, z_D]$ at the SS in Figure 24b, and one finds it is much less than 10% in the low energy region $E_e \lesssim E_c^+$.

B3. CONTRIBUTION FROM THE FLUCTUATION IN THE REACCELERATION

Once we confirm that the contribution of $O[\bar{\epsilon}(\boldsymbol{r})\mathcal{W}_\epsilon(E_e)]$ is approximately given by equation (B5) with the energy loss proportional to $\bar{n}(\boldsymbol{r})$, it is possible to use the path length distribution, $\Pi_n(\boldsymbol{r}; x)$, as presented in Paper I,

$$\Pi_n(\boldsymbol{r}; x) \simeq \frac{2Q_0}{\bar{n}_0 c} \frac{\mathcal{J}_\nu(\omega_\nu, U_\nu)}{J_\nu(U_\nu)} e^{-\bar{\sigma}_r x - |z|/z_D}, \tag{B12}$$

but the slab equation is now slightly cumbersome,

$$\left[c\bar{\sigma}_r E_e^\alpha - \frac{\partial}{\partial E_e} \mathcal{W}_n^*(E_e) - c\zeta_0 \frac{1}{4} \frac{\partial^2}{\partial E_e^2} E_e^{2-\alpha} \right] \cdot F_{r,n}(E_e) = c E_e^{-\gamma}.$$

Remembering that $F_{r,n}^{*(0)}(E_e)$ is a solution of the equation

$$\left[c\bar{\sigma}_r E_e^\alpha - \frac{\partial}{\partial E_e} \mathcal{W}_n^*(E_e) \right] \cdot F_{r,n}^{*(0)}(E_e) = c E_e^{-\gamma},$$

we can write $F_{r,n}(E_e)$ as

$$F_{r,n}(E_e) = F_{r,n}^{*(0)}(E_e) + F_{r,n}^{(1)}(E_e), \tag{B13}$$

with

$$\left[c\bar{\sigma}_r E_e^\alpha - \frac{\partial}{\partial E_e}\mathcal{W}_n^*(E_e)\right] \cdot F_{r,n}^{(1)}(E_e) = c\zeta_0 \frac{1}{4}\frac{\partial^2}{\partial E_e^2} E_e^{2-\alpha} F_{r,n}^{*(0)}(E_e). \tag{B14}$$

The solution for equation (B14) is immediately obtained after the following replacement in equation (28b)

$$cE_e^{-\gamma} \Rightarrow c\zeta_0 \frac{1}{4}\frac{\partial^2}{\partial E_e^2} E_e^{2-\alpha} F_{r,n}^{*(0)}(E_e),$$

and the explicit form is given by

$$\frac{F_{r,n}^{(1)}(E_e)}{F_{r,n}^{*(0)}(E_e)} = c\zeta_0 \frac{1}{4}\int_{E_e}^\infty dE_0 \frac{[E_0^{2-\alpha} F_{r,n}^{*(0)}(E_0)]''}{|\mathcal{W}_n^*(E_e)|F_{r,n}^{*(0)}(E_e)} \, e^{-Y_{r,n}^*(E_e,E_0)},$$

where $Y_{r,n}^*(E_e, E_0)$ is given by replacing $\mathcal{W}_n(E_e)$ in equation (B9) with $\mathcal{W}_n^*(E_e)$.

Now, from equations (B12) and (B13), the electron density in the LE region is given by

$$N_{e,n}(\boldsymbol{r}; E_e) = \frac{2Q_0}{\bar{n}_0}\frac{\mathcal{J}_\nu(\omega_\nu, U_\nu)}{J_\nu(U_\nu)} F_{r,n}(E_e) e^{-|z|/z_D}, \tag{B15}$$

where $F_{r,n}(E_e)$ is given by equation (B13).

Corresponding to equation (26b), we rewrite equation (B15), dividing into three terms as (see also eq. [B11])

$$N_{e,n}(\boldsymbol{r}; E_e) = N_{e,n}^{(0)}(\boldsymbol{r}; E_e) + \tilde{N}_{e,\epsilon}^{(0)}(\boldsymbol{r}; E_e) + N_{e,n}^{(1)}(\boldsymbol{r}; E_e),$$

and in Figure 7 in the text, we present $N_{e,n}^{(1)}/[N_{e,n}^{(0)} + \tilde{N}_{e,\epsilon}^{(0)}]$ against E_e. One finds that the contribution of the fluctuation is effective around GeV region, boosting the electron density without the fluctuation by approximately 25%.

APPENDIX C
EMISSIVITY of γ's COMING FROM INVERSE COMPTON PROCESS

In this appendix, we omit the suffix i for simplicity. The production rate of γ's per unit time due to the bremsstrahlung, $P_{\mathrm{EB}}(\boldsymbol{r}; E_e, E_\gamma) \equiv n(\boldsymbol{r})c\sigma_{\mathrm{EB}}(E_e, E_\gamma)$ in equation (34), must be replaced by

$$P_{\mathrm{IC}}(\boldsymbol{r}; E_e, E_\gamma) \equiv \int_{E_m}^\infty n_{\mathrm{ph}}(\boldsymbol{r}; E_{\mathrm{ph}})c\sigma_{\mathrm{IC}}(E_e, E_\gamma; E_{\mathrm{ph}})dE_{\mathrm{ph}}, \tag{C1}$$

where $E_{\rm ph}$ is the energy of the target photon before electron scattering, and E_m is given by solving equation (A3) with $E_{\rm M} \equiv E_\gamma$ with respect to $E_{\rm ph}$ ($\equiv E_m$),

$$E_m \equiv E_m(E_e, E_\gamma) = k_{\rm B} T_{\rm ph} \Theta_x^2,$$

with

$$\Theta_x \equiv \Theta_x(E_\gamma, T_{\rm ph}; x) = \frac{m_e c^2/2}{\sqrt{(k_{\rm B} T_{\rm ph}) E_\gamma}} \frac{x}{\sqrt{1-x}}; \quad x = \frac{E_\gamma}{E_e},$$

and $\sigma_{\rm IC}(E_e, E_\gamma; E_{\rm ph})$ is the production cross-section of γ's due to IC scattering, which is summarized in the right-hand side of Table 5.

Remarking that the integral range, $E_m \le E_{\rm ph} \le \infty$, in equation (C1) corresponds to $0 \approx (m_e c^2/2 E_e)^2 \le q \le 1$, using a parameter q (Blumenthal & Gould 1970) appearing in the fourth line of the right-hand side of Table 5, equation (C1) is rewritten as

$$P_{\rm IC}(\boldsymbol{r}; E_e, E_\gamma) = \epsilon_{\rm ph}(\boldsymbol{r}) w_{\rm T} \, \Phi_{\rm IC}(x, E_\gamma),$$

with $\epsilon_{\rm ph}$ in units of eVcm^{-3}, and see equation (A5) for $w_{\rm T}$, and

$$\frac{\Phi_{\rm IC}(x, E_\gamma)}{[E_\gamma/{\rm GeV}]} = 9\Big(1 - \frac{1}{x}\Big)^2 \int_0^1 W_{\rm ph}(\Theta_x^2/q)\phi_{\rm IC}(x, q)q\,dq, \qquad (\mathrm{C2})$$

where $W_{\rm ph}(k)$ with $k \equiv \Theta_x^2/q$ corresponds to the two types of energy spectra of the photon gas, the Planck function for the CMB, and the gaussian function for the stellar radiation and the re-emission from the dust grains, and $\phi_{\rm IC}(x, q)$ is given in the right-hand side of Table 5.

REFERENCES

Abdo, A. A., et al. 2009, Phys. Rev. Lett., 102, 181101

Abdo, A. A., et al. 2010a, arXiv:1003.0895v1 [astro-ph.CO] 3 Mar 2010

Abdo, A. A., et al. 2010b, submitted to PRL

Adriani, O., et al. 2009, Phys. Rev. Lett., 102, 051101

Adriani, O., et al. 2010, http://arxiv.org/abs/1007.0821

Aguilar, M., et al. 2002, Phys. Rep., 366, 331

Ahn, H. S., et al. 2005, Proc. 29th Int. Cosmic Ray Conf., (Pune), 3, 57

Ahn, E., Bertone, G., Merritt, D., & Zhang, P. 2007, Phys. Rev. D76, 023517

Ahn, H. S., et al. 2008, Astropart. Phys. 30, 133

Aharonian, F. A., Atoyan, A. M., & Völk, H. J. 1995, A&A, 294, L41

Aharonian, F. A., et al. 2008, arXiv:0811.3894v1 [astro-ph.HE] 24 Nov 2008

Aharonian, F. A., et al. 2009, arXiv:0905.0105v1 [astro-ph.HE] 1 May 2009

Berezhko, E., & Ksenofontov, L. 1999, J. Exp. Theor. Phys., 89, 391

Berezinskii, V. S., et al. 1990, Astrophysics of Cosmic Rays (Amsterdam: North Holland)

Bergström, L. 2000, Rep. Prog. Phys., 63, 793

Bertsch, et al. 1993, ApJ, 416, 587

Bindi, V. 2009, Nucl. Instr. and Meth. A, doi:10.1016/j.nima.2009.10.090

Blumenthal, G. R., & Gould, R. J. 1970, Rev. Mod. Phys., 42, 237

Boezio, M., et al. 2000, ApJ, 532, 653

Caballero, R., et al. 2008, Proc. 30th Int. Cosmic Ray Conf., (Merida), 3, 1313

Case, G., & Bhattacharya, D. 1996, A&AS, 120C, 437

Chang, J. et al. 2008, Nature, 456, 362

Cheng, H. C., Feng, J. L.,& Matchev, K. T. 2002, Phys. Rev. Lett., 89, 211301

Chiang, J., & Mukherjee, R. 1998, ApJ, 496, 752

Clemens, D. P., Sanders, D. B., & Scoville, N. Z. 1988, ApJ, 327, 139

Cordes, J. M., et al. 1991, Nature, 354, 121

Cowsik, R., & Lee, M. A. 1979, ApJ, 228, 297

Cutler, D. J. & Groom, D. E. 1991, ApJ, 376, 322

Davis, A. J., et al. 2000, AIP Conf. Proc., 528, 421

Delahaye, T. et al. 2010, arXiv:1002.1920v1 [astro-ph.HE] 9 Feb 2010

Derbina, V. A., et al. 2005, ApJ, 628, L41

Diplas, A., & Savage, B. D. 1991, ApJ, 377, 126

Dogiel, V. A., & Urysson, A. V. 1988, A&A, 197, 335

DuVernois, M. A., et al. 2001, ApJ, 559, 296

Ellison, D. C., et al. 2000, ApJ, 540, 292

Ferriere, K. M. 2001, Rev. Mod. Phys., 73, 1031

Freudenreich, H. T. 1998, ApJ, 492, 495

Gabici, S., & Blasi, P. 2003, Astropart. Phys., 19, 679

Gaisser, T. K. 1990, Cosmic Rays and Particle Physics (Cambridge: Cambridge Univ. Press)

Ginzburg, V. L. 1979, Theoretical Physics and Astrophysics (Oxford: Pergamon Press)

Ginzburg, V. L., Khazan, Y. A., & Ptuskin, V. S. 1980, Ap&SS, 68, 295

Golden, R. L., et al. 1994, ApJ, 436, 769

Gould, R. J. 1969, Phys. Rev., 185, 72

Heinbach, U., & Simon, M. 1995, ApJ, 441, 209

Henderson, A. P., Jackson, P. D., & Kerr, F. J. 1982, ApJ, 263, 116

Hendrick, S. P., & Reynolds, S. P. 2001, ApJ, 559, 903

Hotta, N. et al. 1980, Phys. Rev., D22, 1

Hunter, S. D., et al. 1997, ApJ, 481, 205

Ishikawa, T. 2010, Master Thesis for Aoyama-Gakuin University

Jones, F. C. 1965, Phys. Rev., 137, B1306

Jones, F. C. 1968, Phys. Rev., 167, 1159

Kasahara, K. 1985, Phys. Rev., D31, 2737

Kappadath, S. C., 1996, A&AS, 120, 619

Kerr, F. J., & Lynden-Bell, D. 1986, MNRAS, 221, 1023

Keshet, U., Waxman, E., & Loeb, A. 2004, J. Cosmol. Astropart. Phys., 04, 006

Kinzer, R. L., Purcell, W. R., & Kurfess, J. D. 1999, ApJ, 515, 215

Kobayashi, T. et al. 1999, Proc. 26th Int. Cosmic Ray Conf., (Salt Lake City), 3, 61

Kobayashi, T., Komori, Y., Yoshida, K. & Nishimura, J. 2004, ApJ, 601, 340

Koch, H. W., & Motz, J. W. 1959, Rev. Mod. Phys., 31, 920

Kodaira, K. 1974, Pub. Astr. Soc. Japan, 26, 255

Kounine, A. 2010, Invited talk at 16th ISVHECRI (Fermilab)

Kulkarni, S. R., Blitz, L., & Heiles, C. 1982, ApJ, 259, L63

Loeb, A., & Waxman, E. 2000, Nature, 405, 156

Mathis, J. S., Mezger, P. G., & Panagia, N. 1983, A&A, 128, 212

Miniati, F. et al. 2000, ApJ, 542, 608

Moskalenko, I. V. et al. 2002, ApJ, 565, 280

Mücke, A., & Pohl, M. 2000, MNRAS, 312, 177

Müller, D. 2009, Proc. 31st Int. Cosmic Ray Conf., (Lodz), in press

Nagashima, K., et al. 1989, Nuovo Cimento, 12C, 695

Nishimura, J. 1964, Prog. Theor. Phys. Suppl. 6, 93

Nishimura, J., Fujii, M. & Taira, T. 1979, Proc. 16th Int. Cosmic Ray Conf., (Kyoto), 1, 488

Nishimura, J. et al. 1980, ApJ, 238, 394

Okamoto, M., & Shibata, T. 1987, Nucl. Instr. Methods A257, 155

Picozza, P., et al. 2007, Proc. 30th Int. Cosmic Ray Conf., (Merida), 2, 19

Pohl, M., & Esposito, J. A. 1998, ApJ, 507, 327

Porter, T. A., et al. 2008, ApJ, 682, 400

Porter, T. A. 2009, Talk at Fermi Symposium (2–5 November, Washington DC)

Ptuskin, V. S., & Ormes, J. F. 1995, Proc. 24th Int. Cosmic Ray Conf., (Rome), 3, 56

Ptuskin, V. S., Jones, F. C., & Ormes, J. F. 1996, ApJ, 465, 972

Reynolds, S. P., & Keohane, J. W. 1999, ApJ, 525, 368

Sakakibara, S. 1965, J. Geomag. Geoelectr., 17, 99

Sato, Y., & Sugimoto, H. 1979, Proc. 16th Int. Cosmic Ray Conf., (Kyoto), 7, 42

Seo, E. S. 2009, Proc. 31st Int. Cosmic Ray Conf., (Lodz), in press

Shen, C. S. 1970, ApJ, 162, L181

Shibata, T., Hareyama, M., Nakazawa, M., & Saito, C. 2004, ApJ, 612, 238 (Paper I)

Shibata, T., Hareyama, M., Nakazawa, M., & Saito, C. 2006, ApJ, 642, 882 (Paper II)

Shibata, T., & Ito, T. 2007, ApJ, 655, 892 (Paper III)

Shibata, T., Honda, N., & Watanabe, J., 2007, Astropart. Phys., 27, 411 (Paper V)

Shibata, T., Futo, Y., & Sekiguchi, S. 2008, ApJ, 678, 907 (Paper IV)

Simon, M., Heinrich, W., & Mathis, K. D. 1986, ApJ, 300, 32

Sreekumar, P., et al. 1998, ApJ, 494, 523

Stecker, F. W., & Jones, F. 1977, ApJ, 217, 843

Stecker, F. W., & Salamon, M. H. 1996, ApJ, 464, 600

Stecker, F. W., Hunter, S. D., & Kniffen, D. A. 2008, Astropart. Phys., 29, 25

Strong, A. W., et al. 1988, A&A, 207, 1

Strong, A. W., & Moskalenko, I. V. 1998, ApJ, 509, 212;
http://www.gamma.mpe.-garching.mpg.de./∼aws/aws.html

Strong, A. W., Moskalenko, I. V. & Ptuskin, V. S. 2007, Annu. Rev. Nucl. Part. Sci. 2007, 57, 285

Strong, A. W., et al. 1999, Astrophys. Lett. Commun., 39, 209

Strong, A. W., Moskalenko, I., & Reimer, O. 2000, ApJ, 537, 763

Strong, A. W., Moskalenko, I., & Reimer, O. 2004, ApJ, 613, 962

Suzuki, R., Watanabe, J., & Shibata, T. 2005, Astropart. Phys., 23, 510

Syrovatskii, S. I., 1959, 36, 17

Torii, S., et al. 2001, ApJ, 559, 973

Torii, S., et al. 2006, Adv. Polar Upper Atmos. Res., 20, 52

Totani, T., & Kitayama, T. 2000, ApJ, 545, 572

Ullio, P., Bergström, L., Edsjö, J., & Lacey, C. 2002, Phys. Rev. D66, 123502

Yamazaki, R., et al. 2006, MNRAS, 371, 1975
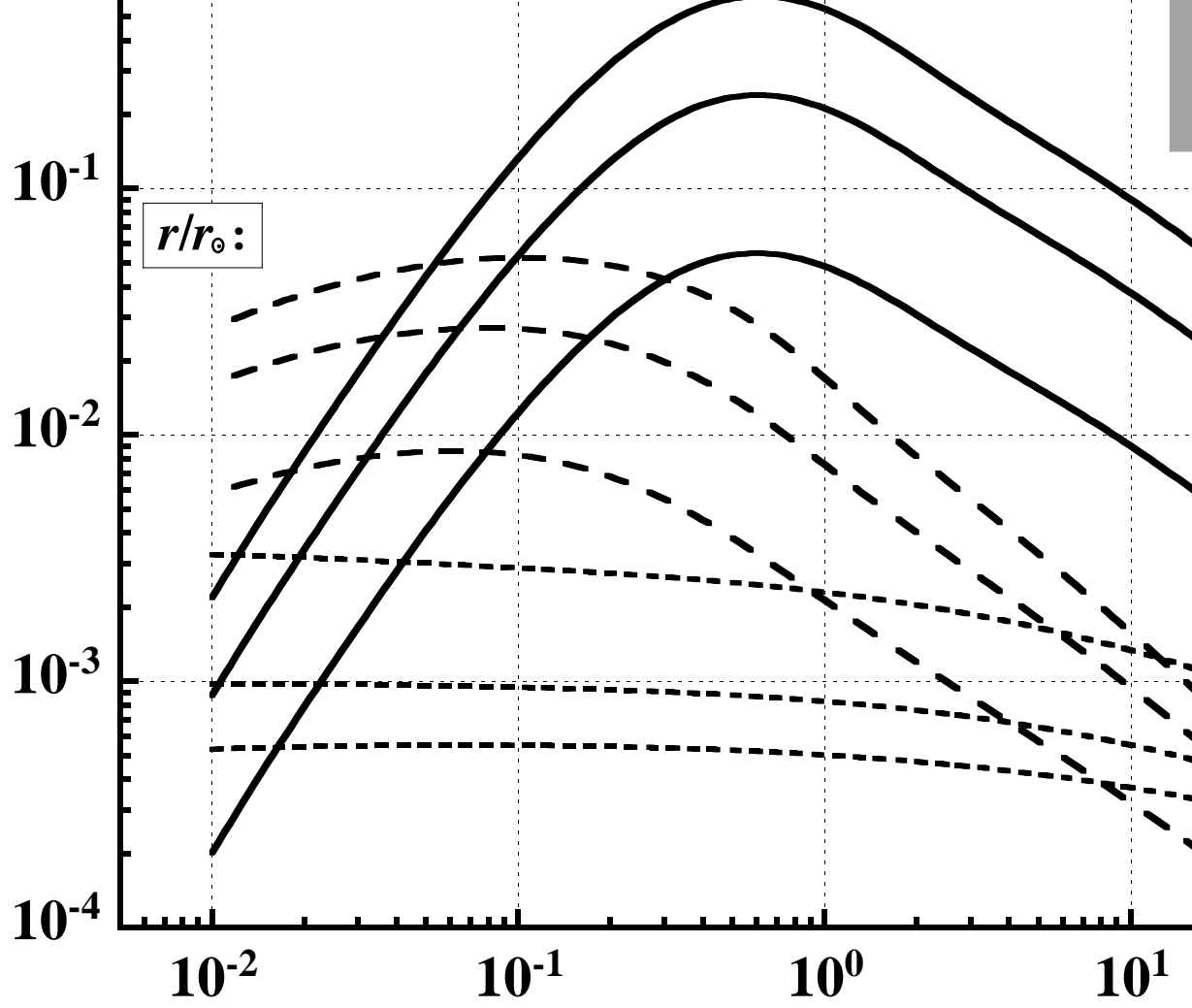
This job requires the 90ms font used in this document.